NASA CONTRACTOR REPORT

NASA CR-1756

NASA CR-1756

THE SIMULATION OF A LARGE JET TRANSPORT AIRCRAFT

Volume I: Mathematical Model

by C. Rodney Blake

Prepared by
THE BOEING COMPANY
Wichita, Kans.
for Ames Research Center

NATIONAL AERONAUTICS AND SPACE ADMINISTRATION • WASHINGTON, D. C. • MARCH 1971

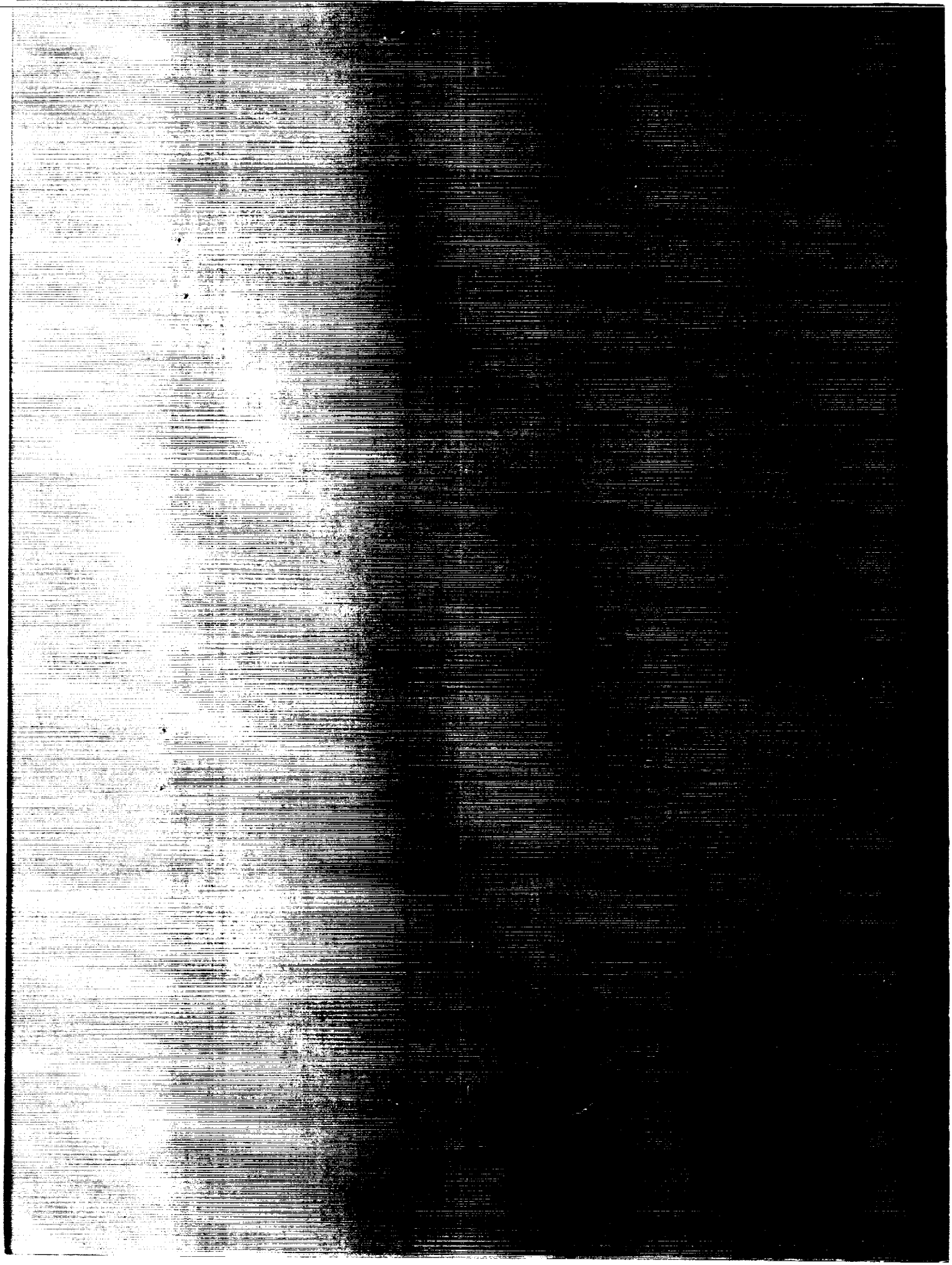

1. Report No.	2. Government Accession No.	3. Recipient's Catalog No.
NASA CR-1756		

4. Title and Subtitle	5. Report Date
"The Simulation of a Large Jet Transport Aircraft Volume I: Mathematical Model"	March 1971
	6. Performing Organization Code

7. Author(s)	8. Performing Organization Report No.
C. Rodney Hanke	10. Work Unit No.

9. Performing Organization Name and Address	11. Contract or Grant No.
The Boeing Company Wichita, Kansas	NAS 2-5524
	13. Type of Report and Period Covered
12. Sponsoring Agency Name and Address	Contractor Report
National Aeronautics and Space Administration Washington, D.C. 20546	14. Sponsoring Agency Code

15. Suppiementary Notes

16. Abstract

The mathematical models used in the manned simulation of a jumbo jet transport aircraft are described. Included are the models of the basic airframe, the longitudinal lateral and directional control systems, the high lift system, the propulsion system, and the landing gear system. In addition, the low speed buffet characteristics and atmospheric model are described.

Included is a list of necessary tests of the simulation to insure validity of the model, of the computer program, and of the quantitative values.

17. Key Words (Suggested by Author(s))	18. Distribution Statement
Simulation Mathematical Model Transport Aircraft	Unclassified-Unlimited

19. Security Classif. (of this report)	20. Security Classif. (of this page)	21. No. of Pages	22. Price*
Unclassified	Unclassified	64	$3.00

*For sale by the National Technical Information Service, Springfield, Virginia 22151

PREFACE

This report summarizes all work conducted by The Boeing Company under Task II of Contract NAS2-5524, "Design for the Simulation of Advanced Aircraft". The National Aeronautics and Space Administration Technical Monitor was Mr. John Dusterberry of the Simulation Science Division. The Boeing Company Project Leader was Mr. C. Rodney Hanke of the Wichita Division Stability, Control and Flying Qualities Organization. Technical assistance was provided by Mr. Robert A. Curnutt of the 747 Aerodynamics Staff, Everett, Washington.

TABLE OF CONTENTS

TABLE OF CONTENTS (CONTINUED)

INTRODUCTION

The Boeing Company provided NASA-Ames Research Center with mathematical models and data to simulate the flying qualities and characteristics of the Boeing 747 on the NASA Flight Simulator For Advanced Aircraft (FSAA).

The contractual report is divided into two volumes. Volume I includes a description of:

1. The work performed under the contract.
2. Generalized equations and approximations used in the simulation.
3. The form of the data furnished to NASA.
4. Nomenclature used for the report.

Volume II contains only limited rights data. These data are to be retained within the Government until The Boeing Company chooses to treat the data as non-proprietary or until September 15, 1971, whichever occurs first.

Boeing and NASA personnel established ground rules for the simulation program; these ground rules resulted in the following conditions of simulation:

1. Flaps-up and flaps-down data were incorporated into one computer program for simulation capability throughout the complete flight envelope.
2. The significant stability derivatives including control effectiveness derivatives were capable of being modified by multiplication factors (normally equal to 1.0).
3. Hydraulic system failures could be simulated by reduced control capability with the multiplication factors described in Item 2.
4. Data describing aircraft system malfunctions (asymmetric flaps, floating control surfaces, etc.) were provided, however, these data were not incorporated in the simulation.
5. Existing NASA digital computer programs were used where possible.
6. The aerodynamic data cards from the Boeing 747 digital simulation were duplicated for NASA and modified for the digital computer format at NASA-Ames. The stored data were observed visually on a scope as a part of the computer program checkout.
7. A single yaw damper system was programmed to drive both rudder segments.
8. Significant blowdown limits were included in the simulation.

9. The rudder ratio changer (limiter) was incorporated in the simulation. Rudder blowdown data were provided but were not required for the simulation.

10. The existing NASA engine simulation program was modified to simulate the 747 propulsion system. The engine simulation included forward, idle, and reverse thrust with first stage compressor RPM, engine pressure ratio, exhaust gas temperature and windmilling drag characteristics.

11. The existing NASA landing gear simulation program was modified to simulate a simplified model of the 747 landing gear. The load equalization system was accounted for by assuming that takeoff rotation occurred about a point midway between the main wing gear and body gear struts. The mathematical model of the main landing gear did not incorporate body gear steering or wing landing gear tilt.

12. Altitude and airspeed system position errors were neglected.

13. The 747 automatic flap retraction system was not incorporated in the simulation. A description of the system was provided to NASA.

14. The 747 autopilot was not included in the simulation but descriptive data on the autopilot were provided to NASA.

15. Constant fuel load was assumed for any simulation run.

NOMENCLATURE

A,B,C	Constants used in stick force program
A.Q.T.	Aft quadrant travel, in.
a	Speed of sound, ft/sec
a_o	Speed of sound, sea level standard, ft/sec
b	Wing span, ft
$\bar{c}$	Wing mean aerodynamic chord, ft
C_D	Airplane drag coefficient, $C_D = \frac{\text{Drag}}{q_D S}$
$C_{D_{Basic}}$	Basic drag coefficient for the rigid airplane at $\alpha_{F.R.L.} = 0^o$, in free air and with the landing gear retracted
C_{D_M}	Drag coefficient at Mach number
C_L	Airplane lift coefficient, $C_L = \frac{\text{Lift}}{q_D S}$
$C_{L_{Basic}}$	Basic lift coefficient for the rigid airplane at $\alpha_{F.R.L.} = 0^o$, in free air and with the landing gear retracted
C_L (c.g. -.25)	Change in pitching moment coefficient due to c.g. variation from 25% M.A.C.
C_ℓ	Airplane rolling moment coefficient, $\frac{\text{Rolling Moment}}{q_D S b}$
C_m	Airplane pitching moment, $C_m = \frac{\text{Pitching Moment}}{q_D S \bar{c}}$
$C_{m_{.25\ Basic}}$	Basic pitching moment coefficient for the rigid airplane at $\alpha_{F.R.L.} = 0^o$, in free air, with the landing gear retracted, and with the c.g. = 25% M.A.C.
C_n	Airplane yawing moment coefficient, $\frac{\text{Yawing Moment}}{q_D S b}$

C_y	Airplane side force coefficient, $\frac{\text{Side Force}}{q_D S}$
c.g.	Airplane center of gravity position as a fraction of the wing mean aerodynamic chord
C_i	Landing gear damping constant
EGT	Exhaust gas temperature
EPR	Engine pressure ratio
F_{B_i}	Tire braking force, lb
F_{G_Z}	Vertical oleo strut force, lb
F_{RX}, F_{RY}, F_{RZ}	Total body axis drag, side, and normal force exerted through the oleo struts, lb.
$F_{RX_{pi}}, F_{RY_{pi}}, F_{RZ_{pi}}$	Body axis drag, side and normal tire force for each oleo strut, lb
F_N	Net thrust, lb
F_{N_G}	Tire force normal to runway, lb
F_s, F_{si}	Tire side force, lb
F.Q.T.	Forward quadrant travel, in
FS	Stick force, lb
$FS_{\substack{\text{Mass} \\ \text{Unbalance}}}$	Stick force due to the mass unbalance of the column, lb
FSAA	Flight Simulator for Advanced Aircraft
$F\mu, F\mu_i$	Tire drag force, lb
FST	Flap screw travel
F.U.T.	Feel unit torque, in-lb
F_{WD}	Engine Windmilling Drag, lb
$F_{X_{B_O}}, F_{Y_{B_O}}, F_{Z_{B_O}}$	Tire forces in body axis for no pitch or roll rotation, lb

$F_{X_{B_\theta}}, F_{Y_{B_\theta}}, F_{Z_{B_\theta}}$	Tire forces in body axis due to pitch rotation only, lb
$F_{X_B}, F_{Y_B}, F_{Z_B}$	Tire forces in body axis due to pitch and roll rotation, lb
g	Acceleration due to gravity, ft/sec^2
G_{T_i}, H_{T_i}	Constants used to determine wheel side force
h	Pressure altitude of the airplane c.g., ft
$h_{B_{c.g._i}}$	Vertical distance from c.g. to force vector created by the tires in contact with the runway, ft
h_G	Height of the tire relative to the runway, ft
h_r	Runway altitude, ft
h_θ	Height of the tire relative to the c.g. due to the pitch angle, ft
h_ϕ	Change in height of the tire relative to the c.g. due to the bank angle, ft
ICAO	International Civil Aviation Organization
K	Drag coefficient interpolation factor
K_B	Braking constant
K_{BM}	Maximum value of braking constant
K_α	Effectiveness factor for elevator and stabilizer
K_{EGT}	Proportionality constant relating exhaust gas temperatures to N_1
K_T	Tire deflection constant
M	Mach number
MA	Mechanical advantage
M.A.C.	Wing mean aerodynamic chord, ft
M_{RX}, M_{RY}, M_{RZ}	Total body axes moments computed from the body axes forces and their distances from the c.g., ft-lb
N_1	Low pressure compressor rotor speed
n_Z	Airplane normal load factor along the Z-axis

P_f	Artificial feel unit pressure, lb/in^2
P_o	Static pressure, sea level standard day, lb/ft^2
p , q, r	Roll, pitch and yaw rates about a reference axes system, radians/sec
q_c	Impact pressure, $q_c = P_{total} - P_{static}$, lb/ft^2
q_D	Dynamic pressure, $q = 1/2\ \rho V^2$, lb/ft^2
r	Tire radius, ft
RPM	Revolutions per minute
S	Wing area, ft^2
$\mathscr{A}_{F.R.L.}$	Horizontal stabilizer angle relative to the fuselage reference line, degrees
T_{AM}	Ambient temperature, ^oR
T_o	Static temperature, sea level standard day, ^oR
T_{t_2}	Total temperature at compressor face, ^oR
T_{t_7}	Turbine discharge total temperature, ^oF
V	True airspeed, ft/sec
V_c	Calibrated airspeed, knots
V_E	Equivalent airspeed, knots
VF_i	Landing gear spring force, lb
V_G	Ground speed, knots
W	Airplane weight, lb
$X_{L_i}, Y_{L_i}, Z_{L_i}$	Distance from c.g. to the end of the fully extended landing gear strut, ft
Y_{E_I}	Effective inboard engine yawing moment arm, ft
Y_{E_O}	Effective outboard engine yawing moment arm, ft
Z_{E_I}	Effective inboard engine pitching moment arm, ft
Z_{E_O}	Effective outboard engine pitching moment arm, ft
α	Angle of attack relative to fuselage reference line, degrees
$\alpha_{W.D.P.}$	Airplane angle of attack relative to the wing design plane, degrees

β	Airplane sideslip angle, degrees
β_G	Airplane sideslip angle relative to ground velocity vector, degrees
δ_{AM}	Ambient pressure ratio, P/P_o
δ_{A_I}	Inboard aileron deflection angle, degrees
δ_{A_O}	Outboard aileron deflection angle, degrees
δ_B	Brake pedal deflection, in
δ_{column}	Control column deflection angle, degrees
δ_e	Elevator deflection angle, degrees
δ_{e_I}	Inboard elevator deflection angle, degrees
δ_{e_O}	Outboard elevator deflection angle, degrees
δ_F	Flap position
δ_P	Rudder pedal deflection, in
δ_R	Rudder deflection angle, degrees
$\delta_{R_{command}}$	Commanded rudder deflection angle, degrees
$\delta_{R_{lower}}$	Lower rudder deflection angle, degrees
$\delta_{R_{max}}$	Maximum rudder deflection angle, degrees
$\delta_{R_{upper}}$	Upper rudder deflection angle, degrees
δ_S	Nose wheel steering angle, degrees
δ_{SBH}	Speed brake handle position, degrees
δ_{SP}	Spoiler deflection angle, degrees
δ_T	Tire deflection, in
δ_W	Control wheel deflection angle, degrees
θ	Temperature ratio, T/T_o
θ_B	Airplane body axis pitch angle, radians
θ_{t_2}	Temperature ratio, T_{t_2} / T_o
ϕ_B	Airplane body axis roll angle, radians

μ_B	Coefficient of braking friction
μ_{roll}	Coefficient of rolling friction
$\frac{\partial \delta_s}{\partial \delta_p}$	Nose wheel steering gearing constant
ΔS_{T_i}	Landing gear oleo strut compression, in
$\frac{dC_D}{d\,\mathscr{a}}\,\mathscr{a}_{F.R.L.}$	Change in basic drag coefficient due to change in stabilizer angle from $\mathscr{a}_{F.R.L.} = 0^o$
$\Delta C_{D_{spoilers}}$	Change in drag coefficient due to spoiler or speedbrake deflection.
$\Delta C_{D_{\substack{landing \\ gear}}}$	Change in drag coefficient due to landing gear extension
$\Delta C_{D_{\substack{ground \\ effect}}}$	Change in drag coefficient due to ground effect
$\Delta C_{D_{sideslip}}$	Change in drag coefficient due to angle of sideslip
$\Delta C_{D_{rudders}}$	Change in drag coefficient due to rudder deflection
$(\Delta C_L)\,\alpha_{W.D.P.} = 0$	Change in basic lift coefficient due to aeroelasticity at $\alpha_{W.D.P.} = 0^o$
$\Delta\left(\frac{dC_L}{d\alpha}\right)\alpha_{W.D.P.}$	Change in basic lift coefficient due to the aeroelastic effect on the rigid airplane basic lift coefficient curve slope
$\frac{dC_L}{d\hat{\dot{\alpha}}}\left(\frac{\dot{\alpha}\bar{c}}{2V}\right)$	Change in lift coefficient due to rate of change of angle of attack
$\frac{dC_L}{d\hat{q}}\left(\frac{q\bar{c}}{2V}\right)$	Change in lift coefficient due to pitch rate
$\frac{dC_L}{dn_z}n_z$	Change in lift coefficient due to aeroelastic inertia relief caused by normal load factor
$K_\alpha\frac{dC_L}{d\,\mathscr{a}}\,\mathscr{a}_{F.R.L.}$	Change in lift coefficient due to change in stabilizer angle from $\mathscr{a}_{F.R.L.} = 0^o$
	Change in lift coefficient due to change in inboard elevator angle from $\delta_{e_I} = 0^o$
$K_\alpha\frac{dC_L}{d\delta_{e_o}}\delta_{e_o}$	Change in lift coefficient due to change in outboard elevator angle from $\delta_{e_o} = 0^o$

$\Delta C_{L_{spoilers}}$	Change in lift coefficient due to spoiler or speedbrake deflection
$\Delta C_{L_{\substack{outboard \\ ailerons}}}$	Change in lift coefficient due to outboard aileron deflection
$\Delta C_{L_{\substack{landing \\ gear}}}$	Change in lift coefficient due to landing gear extension
$\Delta C_{L_{\substack{ground \\ effect}}}$	Change in lift coefficient due to ground effect
$\frac{dC_\ell}{d\beta}\beta$	Rolling moment coefficient due to angle of sideslip
$\frac{dC_\ell}{d\hat{p}}\left(\frac{p_s b}{2V}\right)$	Rolling moment coefficient due to roll rate about the stability axis
$\frac{dC_\ell}{d\hat{r}}\left(\frac{r_s b}{2V}\right)$	Rolling moment coefficient due to yaw rate about the stability axis
$\Delta C_{\ell_{spoilers}}$	Rolling moment coefficient due to spoiler deflection
$\Delta C_{\ell_{\substack{inboard \\ ailerons}}}$	Rolling moment coefficient due to inboard aileron deflection
$\Delta C_{\ell_{\substack{outboard \\ ailerons}}}$	Rolling moment coefficient due to outboard aileron deflection
$\Delta C_{\ell_{rudders}}$	Rolling moment coefficient due to rudder deflection
$\left(\Delta C_{m_{.25}}\right)_{\alpha_{W.D.P.}=0}$	Change in pitching moment coefficient at $\alpha_{W.D.P.} = 0$ due to aeroelasticity
$\Delta\left(\frac{dCm}{d\alpha}.25\right)\alpha_{W.D.P.}$	Change in pitching moment coefficient due to the aeroelastic effect on the rigid airplane basic pitching moment coefficient curve slope
$\frac{dCm}{d\hat{\dot{\alpha}}}\left(\frac{\dot{\alpha}\bar{c}}{2V}\right)$	Change in pitching moment coefficient due to rate of change of angle of attack
$\frac{dCm}{d\hat{q}}\left(\frac{q\bar{c}}{2V}\right)$	Change in pitching moment coefficient due to pitch rate
$\frac{dCm}{dn_z}n_z$	Change in pitching moment coefficient due to aeroelastic inertia relief caused by normal load factor

$K_\alpha \frac{dCm}{d\alpha}_{.25} \alpha_{F.R.L.}$	Change in pitching moment coefficient due to change in stabilizer angle from $\alpha_{F.R.L.} = 0^o$
$K_\alpha \frac{dCm}{d\delta_{e_I}}_{.25} \delta_{e_I}$	Change in pitching moment coefficient due to change in inboard elevator angle from $\delta_{e_I} = 0^o$
$K_\alpha \frac{dCm}{d\delta_{e_O}}_{.25} \delta_{e_O}$	Change in pitching moment coefficient due to change in outboard elevator angle from $\delta_{e_O} = 0^o$
$\Delta C_{m_{.25_{spoilers}}}$	Change in pitching moment coefficient due to spoiler or speed brake deflection
$\Delta C_{m_{.25_{\substack{inboard \\ ailerons}}}}$	Change in pitching moment coefficient due to inboard aileron deflection
$\Delta C_{m_{.25_{\substack{outboard \\ ailerons}}}}$	Change in pitching moment coefficient due to outboard aileron deflection
$\Delta C_{m_{.25_{\substack{landing \\ gear}}}}$	Change in pitching moment coefficient due to landing gear extension
$\Delta C_{m_{.25_{\substack{ground \\ effect}}}}$	Change in pitching moment coefficient due to ground effect
$\Delta C_{m_{.25_{sideslip}}}$	Change in pitching moment coefficient due to angle of sideslip
$\Delta C_{m_{.25_{rudders}}}$	Change in pitching moment coefficient due to rudder deflection
$\frac{dCn}{d\beta} \beta$	Yawing moment coefficient due to angle of sideslip
$\frac{dCn}{d\hat{\dot{\beta}}} \left(\frac{\dot{\beta} b}{2V}\right)$	Yawing moment coefficient due to rate of change of sideslip angle
$\frac{dCn}{d\hat{p}} \left(\frac{p_s b}{2V}\right)$	Yawing moment coefficient due to roll rate about the stability axis
$\frac{dCn}{d\hat{r}} \left(\frac{r_s b}{2V}\right)$	Yawing moment coefficient due to yaw rate about the stability axis

$\Delta C_{n_{spoilers}}$	Yawing moment coefficient due to spoiler deflection
$\Delta C_{n_{\substack{inboard \\ ailerons}}}$	Yawing moment coefficient due to inboard aileron deflection
$\Delta C_{n_{\substack{outboard \\ ailerons}}}$	Yawing moment coefficient due to outboard aileron deflection
$\Delta C_{n_{rudders}}$	Yawing moment coefficient due to rudder deflection
$\frac{dC_Y}{d\beta}\beta$	Side force coefficient due to angle of sideslip
$\frac{dC_Y}{d\hat{p}}\left(\frac{p_s b}{2V}\right)$	Side force coefficient due to roll rate about the stability axis
$\frac{dC_Y}{d\hat{r}}\left(\frac{r_s b}{2V}\right)$	Side force coefficient due to yaw rate about the stability axis
$\Delta C_{Y_{spoilers}}$	Side force coefficient due to spoiler deflection
$\Delta C_{Y_{rudders}}$	Side force coefficient due to rudder deflection
$\frac{d(\ )}{dt} = (\cdot)$	Time derivative operation

Landing Gear Designation

$i = 1$	Nose Gear
$i = 2$	Left main landing gear
$i = 3$	Right main gear

GENERAL AIRCRAFT DESCRIPTION

The Boeing 747 is a four-fanjet intercontinental transport designed to operate from existing international airports. High lift for low speed flight is obtained with wing triple-slotted trailing flaps and Krueger type leading edge flaps. The Krueger flaps outboard of the inboard nacelle are cambered and slotted while the inboard Krueger flaps are standard unslotted. A movable stabilizer with four elevator segments provides longitudinal control for the aircraft. The lateral control is obtained with five spoiler panels, an inboard aileron between the inboard and outboard flaps, and an outboard aileron which only operates when the flaps are down. The five spoiler panels on each wing which are used for lateral control also operate symmetrically as speedbrakes in conjunction with the sixth spoiler panel. Directional control is obtained with a two-segment rudder. A general arrangement drawing of the controls and geometric dimensions of the aircraft is shown in Figure 1. A summary of the basic reference areas and geometric dimensions for the simulation is shown in Table 1.

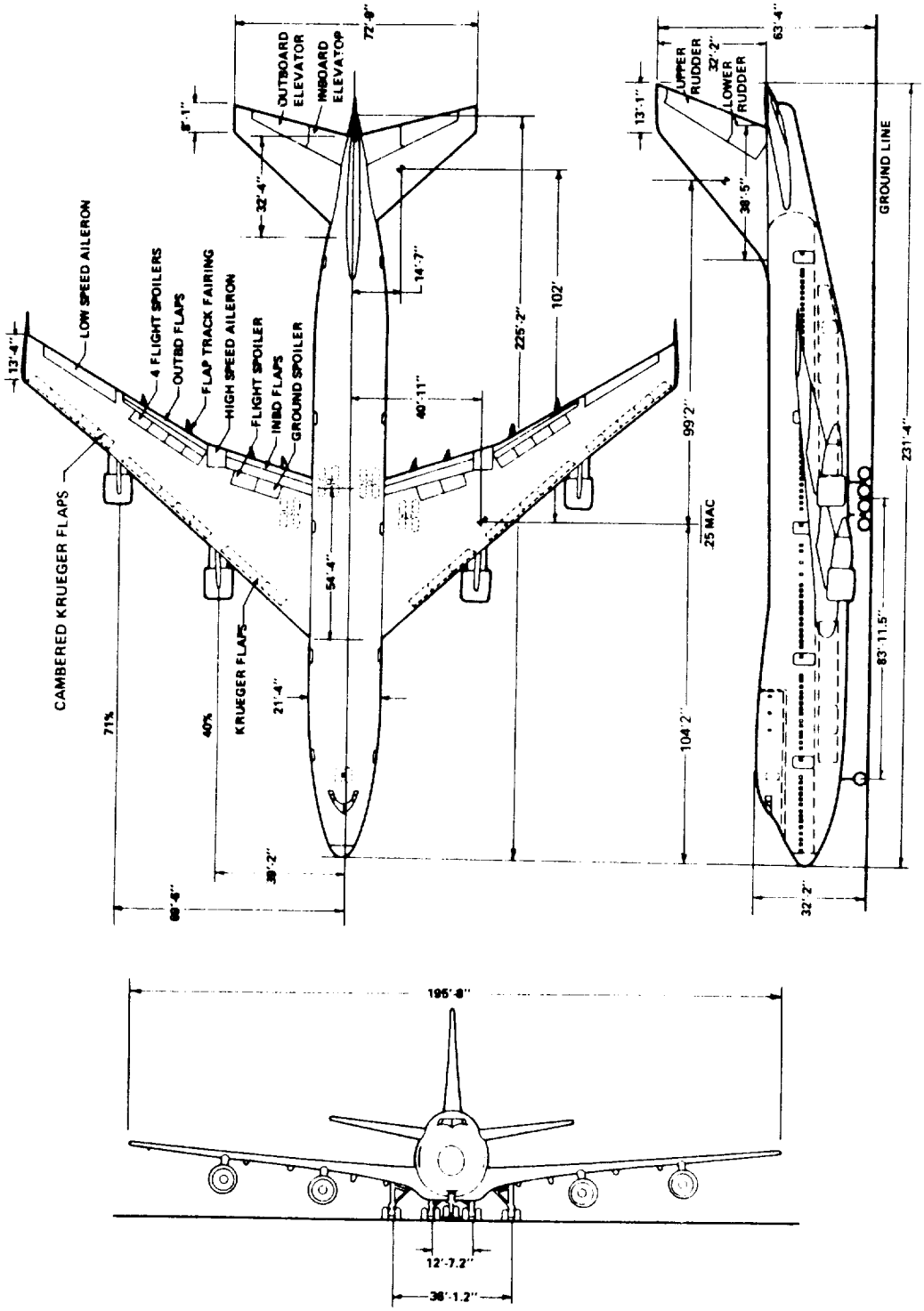

747 THREE-VIEW

FIGURE 1

ITEM	VALUE	DIMENSION
Wing Area (S)	5500	$Ft.^2$
Wing Mean Aerodynamic Chord (MAC)	27.3	Ft.
Wing Span (b)	195.7	Ft.
Wheel Base		
Wing Gear	79	Ft.
Body Gear	89	Ft.
Wheel Tread		
Wing Gear	36.2	Ft.
Body Gear	12.5	Ft.
Pilots Station to .25 MAC (ΔX)	86	Ft.
Pilots Station to Aircraft Centerline (ΔY)	1.7	Ft.
Pilots Station to Aircraft c.g. (ΔZ)	10	Ft.

SUMMARY OF AREAS AND DIMENSIONS

TABLE 1

AIRFRAME SIX DEGREE-OF-FREEDOM MODEL

This section contains the general form of equations for computing force and moment coefficients created by aerodynamic loads on the airplane. Each equation is written as a function of its significant variables. The NASA multiplication factors which can be used to modify the basic stability derivatives (ground rule 2 of the Introduction) are not included in these equations. The aerodynamic data in stability axes for these equations are included in Volume II of this report. The dimensionless force and moment coefficients (C_L, C_D, C_m, C_ℓ, C_n and C_y) were converted into dimensional forces and moments. These forces and moments were used in an existing NASA digital computer program to obtain six degree-of-freedom airframe response. Sign conventions for the control surface deflections and the aerodynamic coefficients are shown in Figure 2.

Lift Force Coefficient

The dimensionless aerodynamic lift force coefficient was computed by the following general equation for a given angle of attack:

$$
\begin{aligned}
C_L = {} & C_{L_{Basic}} + (\Delta C_L)_{\alpha_{W.D.P.}=0} + \Delta\left(\frac{dC_L}{d\alpha}\right)_{\alpha_{W.D.P.}} \\
& + \frac{dC_L}{d\left(\frac{\dot{\alpha}\bar{c}}{2V}\right)} + \frac{dC_L}{d\left(\frac{q\bar{c}}{2V}\right)} + \frac{dC_L}{dn_z} n_z + K_\alpha \frac{dC_L}{d\alpha}_{F.R.L.} \\
& + K_\alpha \frac{dC_L}{d\delta_{e_I}} \delta_{e_I} + K_\alpha \frac{dC_L}{d\delta_{e_O}} \delta_{e_O} + \Delta C_{L_{spoilers}} \\
& + \Delta C_{L_{\substack{outboard \\ ailerons}}} + \Delta C_{L_{\substack{landing \\ gear}}} + \Delta C_{L_{\substack{ground \\ effect}}} .
\end{aligned}
$$

The aerodynamic lift force data and detailed equations for obtaining the stability derivatives and control surface parameters are included in Section 2, Volume II of this report.

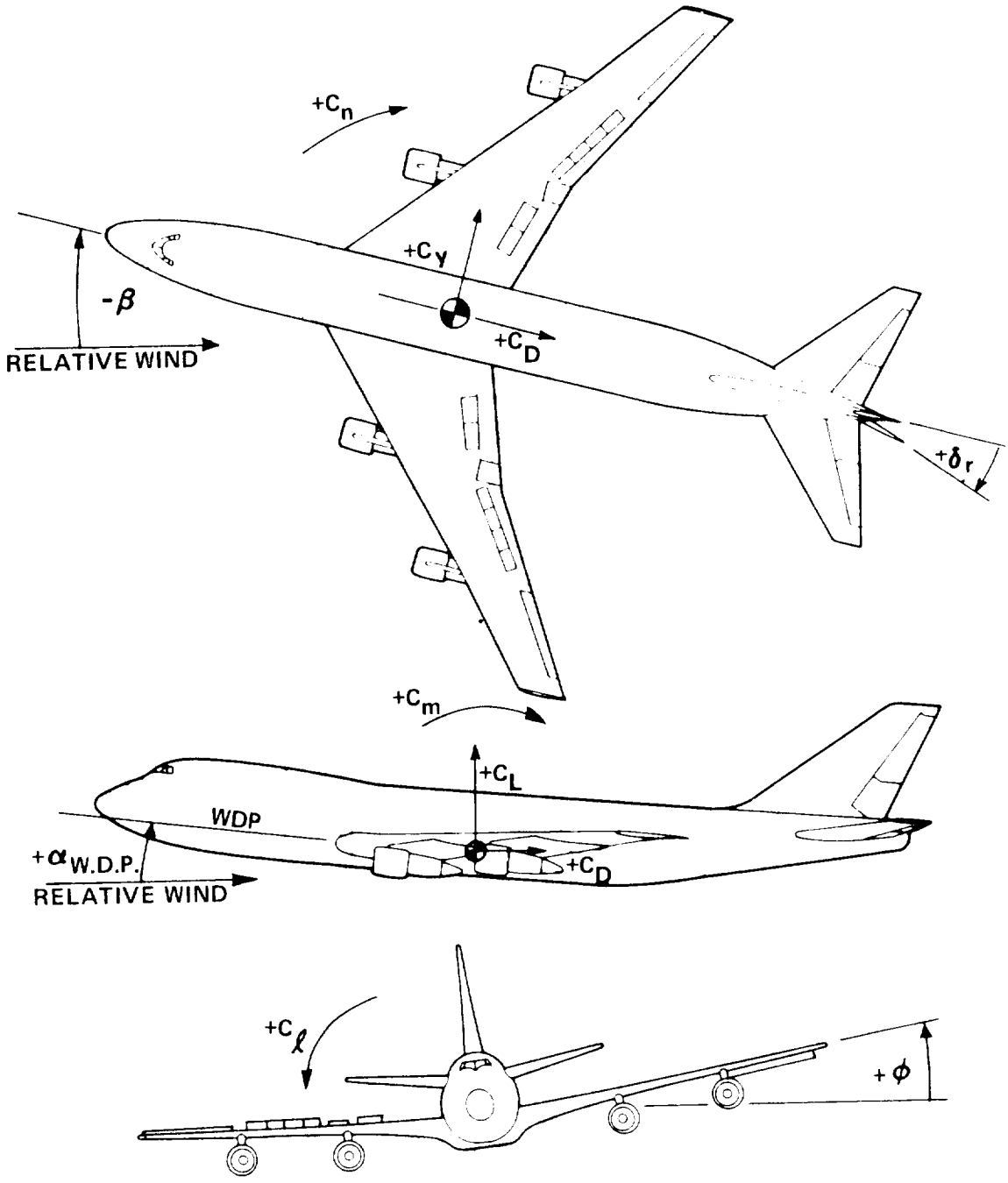

ALL CONTROL SURFACE TRAILING EDGE DOWN DEFLECTIONS ARE POSITIVE

RIGHT WING SPOILER DEFLECTION IS POSITIVE

SIGN CONVENTION
(STABILITY AXES)

FIGURE 2

Drag Force Coefficient

The dimensionless aerodynamic drag force coefficient was computed by the following general equation for a given angle of attack:

$$C_D = K\left[C_{D_{Basic}} + \frac{dC_D}{d\alpha}\alpha_{F.R.L.}\right] + \left[1-K\right]\left[C_D\right]_M + \Delta C_{D_{spoilers}} + \Delta C_{D_{\substack{landing\\gear}}} + \Delta C_{D_{\substack{ground\\effect}}} + \Delta C_{D_{sideslip}} + \Delta C_{D_{rudders}} .$$

The aerodynamic drag force data and detailed equations for obtaining the stability derivatives and control surface parameters are included in Section 3, Volume II of this report.

Pitching Moment Coefficient

The dimensionless aerodynamic pitching moment coefficient was computed by the following general equation for a given angle of attack:

$$C_m = C_{m_{.25\ Basic}} + \left(\Delta C_{m_{.25}}\right)_{\alpha\ W.D.P.=0} + \Delta\left(\frac{dCm}{d\alpha}.25\right)\alpha_{W.D.P.} + C_L\ (c.g.-.25) + \frac{dCm}{d\hat{\alpha}}\left(\frac{\dot{\alpha}\bar{c}}{2V}\right) + \frac{dCm}{d\hat{q}}\left(\frac{q\bar{c}}{2V}\right) + \frac{dCm}{dn_z}n_z + K_\alpha\frac{dCm}{d\alpha}.25\alpha_{F.R.L.} + K_\alpha\frac{dCm}{d\delta_{e_I}}.25\,\delta_{e_I} + K_\alpha\frac{dCm}{d\delta_{e_o}}.25\,\delta_{e_o} + \Delta C_{m_{.25_{spoilers}}} + \Delta C_{m_{.25_{\substack{inboard\\ailerons}}}} + \Delta C_{m_{.25_{\substack{outboard\\ailerons}}}} + \Delta C_{m_{.25_{\substack{landing\\gear}}}} + \Delta C_{m_{.25_{\substack{ground\\effect}}}} + \Delta C_{m_{.25_{sideslip}}} + \Delta C_{m_{.25_{rudders}}}$$

The aerodynamic pitching moment data and detailed equations for obtaining the stability derivatives and control surface parameters are included in Section 4, Volume II of this report.

Rolling Moment Coefficient

The dimensionless aerodynamic rolling moment coefficient was computed by the following general equation for a given angle of attack:

$$C_{\ell} = \frac{dC_{\ell}}{d\beta}\beta + \frac{dC_{\ell}}{d\hat{p}}\left(\frac{p_s b}{2V}\right) + \frac{dC_{\ell}}{d\hat{r}}\left(\frac{r_s b}{2V}\right) + \Delta C_{\ell_{spoilers}} + \Delta C_{\ell_{\substack{inboard \\ ailerons}}} + \Delta C_{\ell_{\substack{outboard \\ ailerons}}} + \Delta C_{\ell_{rudders}}.$$

The aerodynamic rolling moment data and detailed equations for obtaining the stability derivatives and control surface parameters are included in Section 5, Volume II of this report.

Yawing Moment Coefficient

The dimensionless aerodynamic yawing moment coefficient was computed by the following general equation for a given angle of attack:

$$C_n = \frac{dCn}{d\beta}\beta + \frac{dCn}{d\hat{\dot{\beta}}}\left(\frac{\dot{\beta} b}{2V}\right) + \frac{dCn}{d\hat{p}}\left(\frac{p_s b}{2V}\right) + \frac{dCn}{d\hat{r}}\left(\frac{r_s b}{2V}\right) + \Delta C_{n_{spoilers}} + \Delta C_{n_{\substack{inboard \\ ailerons}}} + \Delta C_{n_{\substack{outboard \\ ailerons}}} + \Delta C_{n_{rudders}}.$$

The aerodynamic yawing moment data and detailed equations for obtaining the stability derivatives and control surface parameters are included in Section 6, Volume II of this report.

Side Force Coefficient

The dimensionless aerodynamic side force coefficient was computed by the following general equation for a given angle of attack:

$$C_Y = \frac{dCy}{d\beta}\beta + \frac{dCy}{d\hat{p}}\left(\frac{p_s b}{2V}\right) + \frac{dCy}{d\hat{r}}\left(\frac{r_s b}{2V}\right)$$
$$+ \Delta C_{Y_{spoilers}} + \Delta C_{Y_{rudders}}.$$

The aerodynamic side force data and detailed equations for obtaining the stability derivatives and control surface parameters are included in Section 7, Volume II of this report.

LONGITUDINAL CONTROL SYSTEM

General Description

The longitudinal control system consists of two inboard and two outboard elevators and a movable horizontal stabilizer.

Under normal operation, the outboard elevator angle is equal to the inboard elevator angle at speeds below blowdown. The elevators are downrigged 2^{o} from the faired position. The control column is directly linked to the forward quadrant control mechanism. The mechanical rotation of the forward quadrant is transmitted through the control cables to the aft quadrant which controls the elevator actuators. The elevators are fully powered through irreversible hydraulic actuators connected directly to the elevators. Actual elevator deflection is limited by the hydraulic rate, the mechanical stop, or the pressure blowdown.

Control forces are synthesized in an artificial force feel unit which operates as a function of dynamic pressure and stabilizer position.

Pitch trim is available through the movable horizontal stabilizer. The stabilizer position is controlled by thumb switches on the pilot and copilot control wheels. The trim command actuates hydraulic motors which drive a jackscrew mechanism at a rate which is a function of impact pressure.

NASA Longitudinal Control Model and Approximations

A block diagram of the simulated elevator control system and the computed stick force is shown in Figure 3. The column travel in the FSAA was slightly less than the column travel in the 747. For this simulation, the column deflection of the FSAA was scaled up in the computer program such that full deflection of the FSAA column represented full deflection of the 747 column. The control column deflection in the simulator cab was converted into an equivalent forward quadrant angle on the digital computer. Aft quadrant travel was equal to the forward quadrant travel minus the amount due to cable stretch. The cable stretch was proportional to the torque generated by the artificial feel unit. The aft quadrant was converted into an elevator command which was converted into true elevator position through rate and blowdown limiters. The torque of the force feel unit was obtained as a function of aft quadrant travel and feel unit pressure. The feel unit torque was converted into cable stretch and cable load by conversion constants. The stick force produced by the cable load and the mechanical advantage was added to the stick force from the column mass balance to form the computed stick force. The computed stick force was input to the FSAA control loader to provide the pilot with the proper longitudinal force feel characteristics.

The stall warning was provided by a stick shaker model which was activated as a function of angle of attack and flap angle. The data are included in Section 2, Volume II of this report. The frequency and amplitude of the stick shaker model were varied until the evaluation pilot felt the control column "shake" was representative of the 747.

Data for the stick force simulation is presented in Section 8, Volume II of this report.

The stabilizer position was controlled by thumb switches on the pilot and copilot control wheels. A trim command drove the stabilizer trim rate as a function of impact pressure, Figure 4.

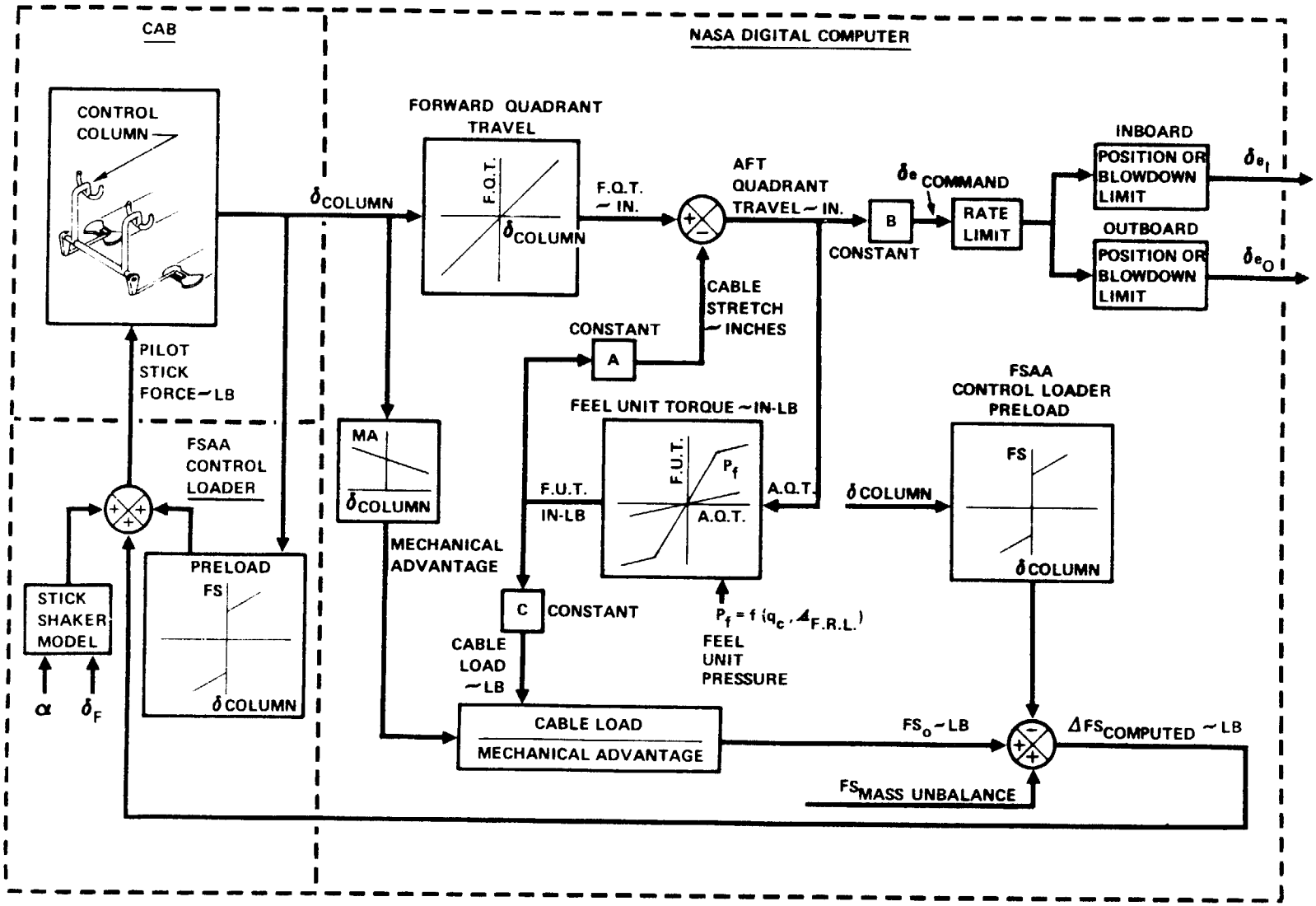

ELEVATOR AND STICK FORCE MODEL

FIGURE 3

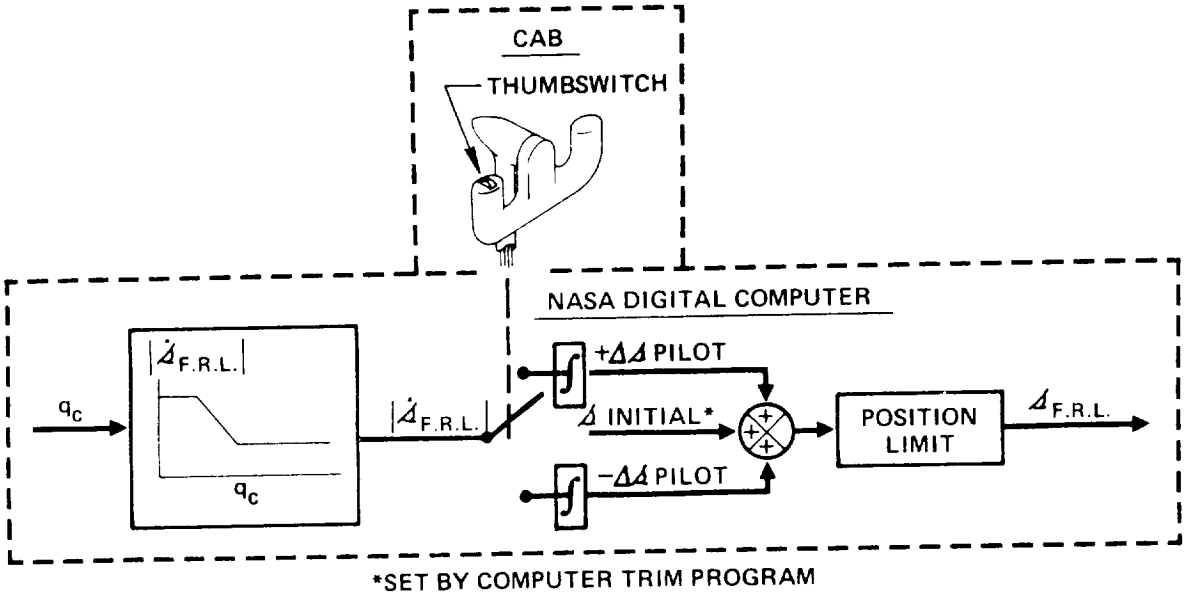

STABILIZER TRIM
FIGURE 4

LATERAL CONTROL SYSTEM

General Description

The lateral control system is a combination of inboard ailerons, outboard ailerons and spoilers. The spoilers can also be used as speedbrakes. Pilot input to the dual tandem central control actuators is provided by a cable system from each of the pilot and copilot control wheels. The actuators drive independent cable systems to the left and right wing lateral control surfaces.

The inboard ailerons operate in all flight regimes while the outboard ailerons operate only when the flaps are down. The outboard ailerons are locked out when the flaps are up.

There are six spoiler panels on each wing. Five panels are modulated by wheel and speedbrake commands and one panel on each wing is controlled by the speedbrake commands. The speedbrake handle is located on the center aisle stand. The five modulated panels on each wing are controlled from "mixer" boxes which sum the inputs from the pilot's wheel and speedbrake inputs. Wheel inputs will move the modulated spoiler panels up or down within the travel limits at any speedbrake setting.

Control wheel force is synthesized by a spring, as a function of wheel deflection.

NASA Lateral Control Model And Approximations

A block diagram of the simulated lateral control system is shown on Figure 5. The wheel deflection in the simulator cab was converted into an equivalent spoiler and aileron angle on the digital computer. Each spoiler bank deflection was computed separately. The block diagram of Figure 5 illustrates the deflection of only one spoiler panel as a function of wheel deflection for speedbrakes up and down. The commanded spoiler angle was input to the spoiler rate and deflection limiter and the output was the actual deflection for each spoiler panel.

Also shown in Figure 5 is the aileron command as a function of wheel deflection. The ailerons were rate limited. Aileron blowdown was neglected for this simulation. Aileron blowdown information is presented in Section 9 Volume II of this report. On the aircraft, the inboard ailerons are not blowdown limited during normal operations, however, the outboard ailerons can have slightly reduced authority due to blowdown near the flap placard speeds.

For the NASA simulation, wheel forces were approximated by a breakout force and a constant gradient programmed on the FSAA control loader.

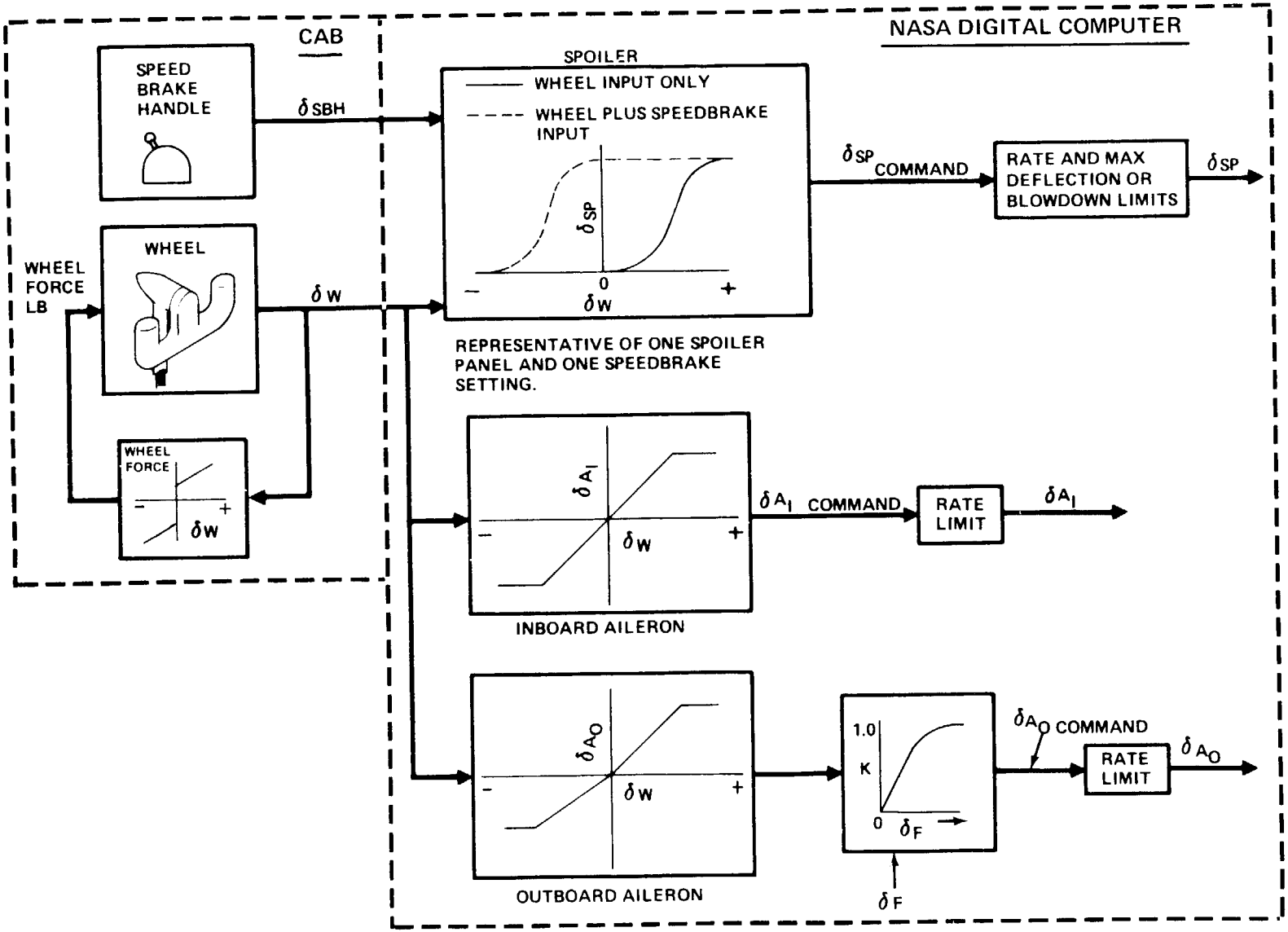

LATERAL CONTROL SYSTEM MODEL
FIGURE 5

DIRECTIONAL CONTROL SYSTEM

General Description

The directional control system consists of two rudder segments, upper and lower, each being controlled by a dual tandem actuator. Both rudder segments move together under normal operation. Rudder pedal movement is converted to rudder deflection by cables linking the forward quadrant mechanism to two ratio changers located in the empennage. The rudder ratio changer is programmed to limit maximum rudder travel to ensure safe structural limits at high airspeeds. The rudders are fully powered through irreversible dual source hydraulic actuators which are controlled by the rudder ratio changers. The actual rudder deflection is limited by the hydraulic rate limit, the pressure limit and the ratio changer.

A yaw damper is incorporated which commands rudder proportional to yaw rate and bank angle. For normal operation, the yaw damper drives both rudder segments together. Turn coordination, operative only with flaps down, is achieved by deflecting the rudder through the yaw damper. The yaw damper has its own rudder rate and deflection limits. The rudder commanded by the yaw damper does not result in any movement of the rudder pedals and does not affect the normal operation of the rudder.

Rudder pedal feel forces are provided by mechanical springs and are proportional to rudder pedal movement. Since the ratio changer reduces the rudder deflection with pedal movement as a function of airspeed, the pedal displacement and force to obtain a given rudder deflection is variable with airspeed.

NASA Directional Control Model and Approximations

A block diagram of the simulated rudder control system is shown in Figure 6. The rudder pedal deflection in the cab was converted into a fractional rudder command on the digital computer ($\delta R/\delta RMAX$). The maximum rudder deflection allowed by the rudder ratio changer was programmed as a function of calibrated airspeed. The commanded rudder deflection was obtained by multiplying the fractional rudder command by the maximum allowable rudder angle as determined by the ratio changer. The pilot's rudder command was then rate limited to obtain actual rudder deflection (less yaw damper inputs). For the NASA simulation, the maximum rudder deflection was assumed to be determined by the rudder ratio changer and not the hydraulic pressure limit (blowdown). Under most flight conditions, the actual aircraft rudder is ratio changer limited instead of hydraulic pressure limited. Rudder blowdown data is included in Section 10, Volume II of this report.

For the NASA simulation, rudder pedal forces were approximated by a breakout force and a constant gradient programmed on the FSAA control loader.

The rudder deflection due to the yaw damper system was position and rate limited, and then added to the rudder deflection due to the pilot inputs to obtain the total rudder deflection. The upper and lower rudder angles were both computed by the same mathematical functions. A block diagram with transfer functions of the yaw damper and turn coordinator systems are included in Section 10, Volume II of this report.

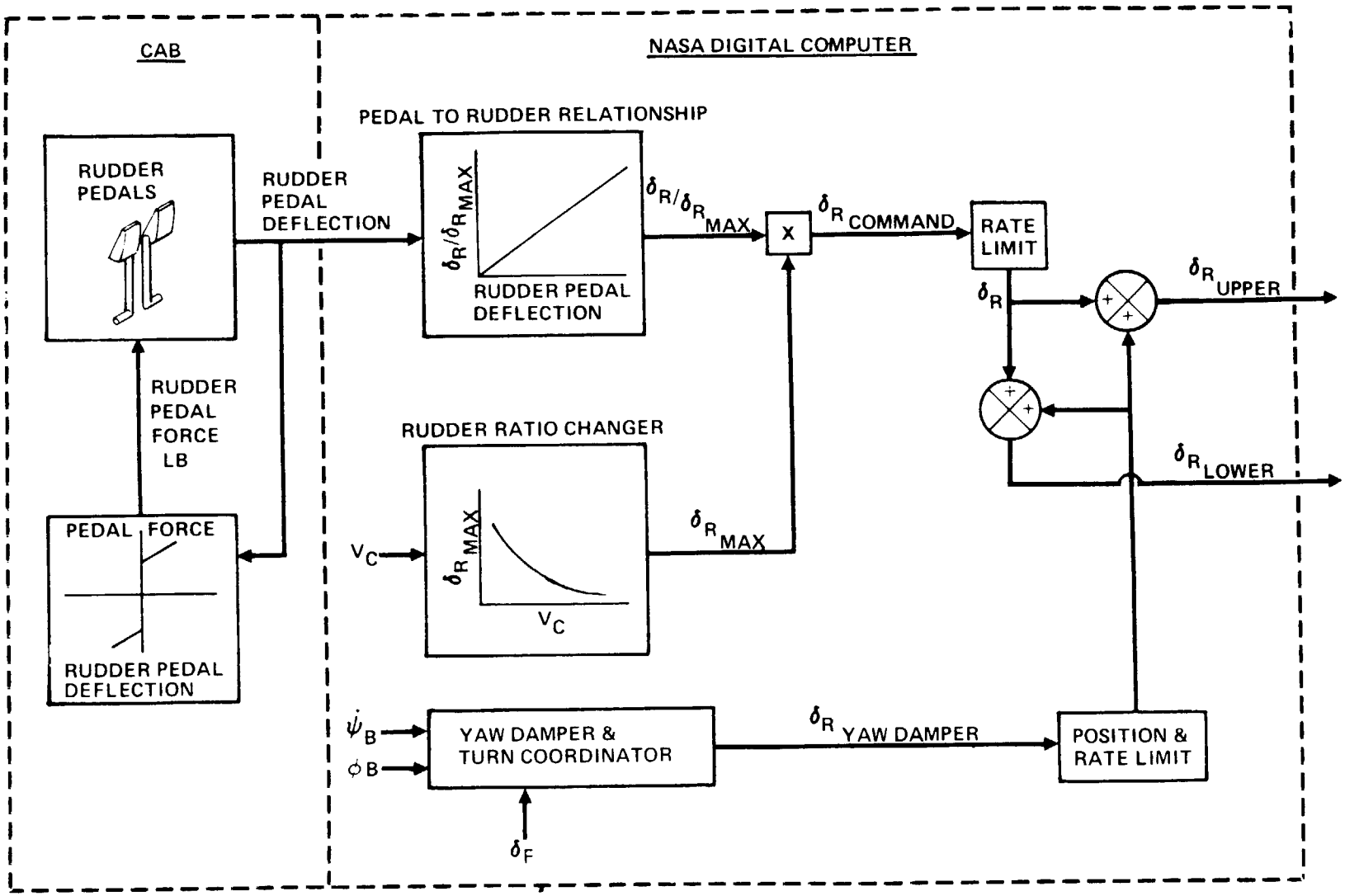

DIRECTIONAL CONTROL MODEL
FIGURE 6

HIGH LIFT SYSTEM

General Description

The 747 flap system consists of two inboard and two outboard triple slotted trailing edge flaps and Krueger type leading edge flaps, Figure 7. The Krueger flaps outboard of the inboard nacelle are cambered and slotted while the inboard Krueger flaps are standard unslotted. During extension, the outboard Krueger flaps alter in shape, flexing from a near-flat to a curved surface. The leading edge flaps are either in the full extended or retracted position as a function of the trailing edge flap position.

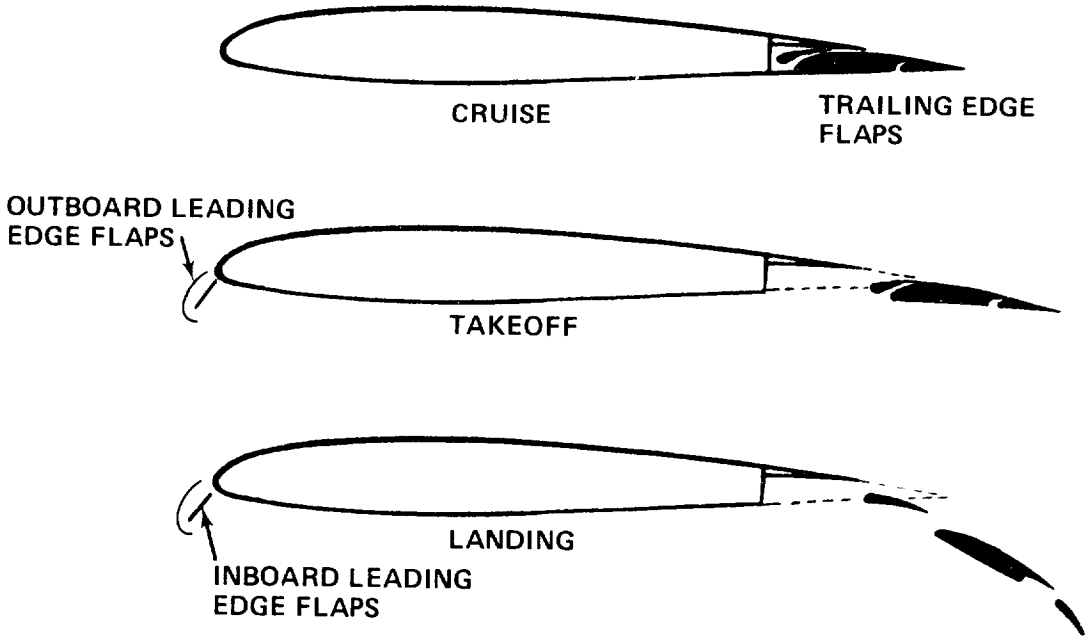

FLAP CONFIGURATION

FIGURE 7

NASA High Lift Model and Approximations

The 747 flap control lever has seven detents, 0, 1, 5, 10, 20, 25 and 30 for flap position commands. The FSAA flap control lever had five detents. Because position 1 and 5 are leading edge check positions, the five available detents were used to command flap positions 0, 10, 20, 25 and 30. FSAA flap control lever positions between 0 and 10 gave a continuous flap position between 0 and 10. For FSAA flap control lever position greater than 10, flap positions were discretely commanded for the nearest detent position.

A block diagram of the simulated flap control system is shown in Figure 8. The FSAA flap control lever commanded flap screw travel as a function of commanded flap position. The simulated flap screw was driven at a constant rate during flap extension and retraction.

All flaps down aerodynamic data presented in Volume II of this report include effects of leading edge flaps.

Aerodynamic data to simulate asymmetric flap conditions are presented in Volume II of this report. However, these data were not required for the simulation.

The flap auto-retraction system was not included in the simulation.

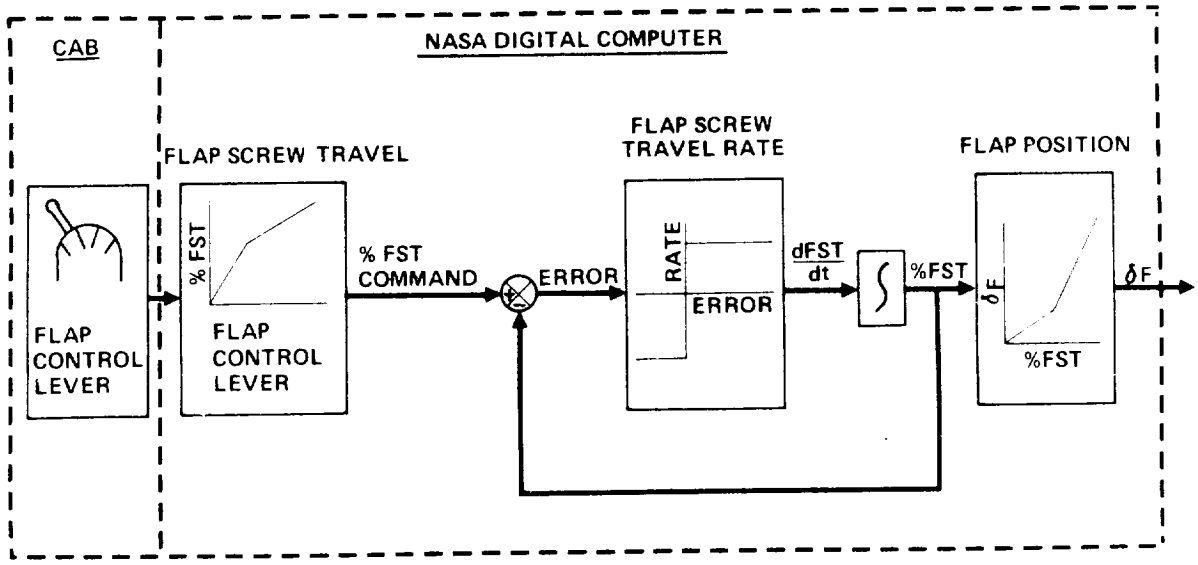

HIGH LIFT MODEL

FIGURE 8

LOW SPEED BUFFET MODEL

The NASA buffet program was tailored to match the 747 buffet characteristics. Cab buffet intensity was a function of angle of attack, flap position, and spoiler deflection. The intensity associated with angle of attack and spoiler deflection was varied until the pilot felt the buffet was representative of the 747.

Airplane buffet data is presented in Volume II of this report.

General Description

The 747 aircraft is powered by four Pratt and Whitney JT9D-3 engines having a takeoff thrust rating of 43,500 pounds on a standard sea level day. The JT9D-3 engine is an axial flow, twin spool, high compression, high bypass ratio, turbofan engine. The engines are pod mounted at approximately 40 and 71 percent of the wing semi-span.

Two thrust reversers are provided on each engine, one to reverse the bypass fan exhaust and one to reverse the turbine exhaust. A general description of the engine in normal and reverse thrust modes is shown in Figure 9.

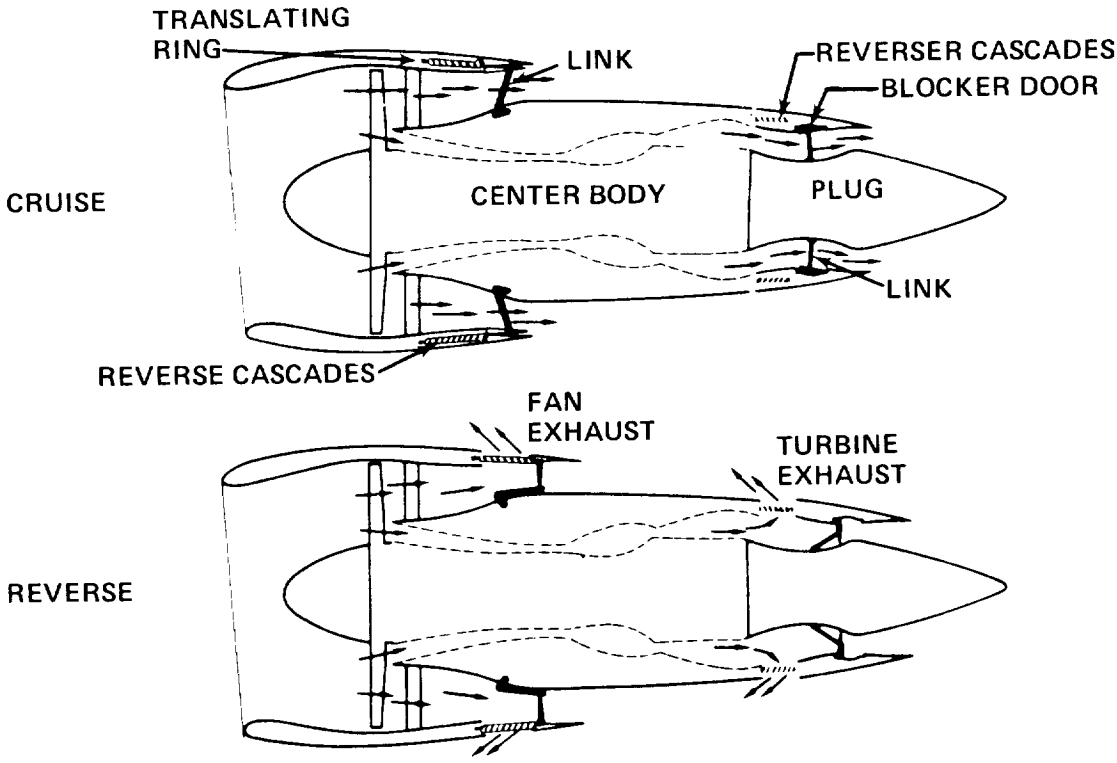

FIGURE 9

Both thrust reversers have a translating ring which is located in the outer wall of the nozzle annulus. The plug or centerbody forms the inner wall of the nozzle. During thrust reversal, the translating ring moves to the rear to block the rearward flow of the exhaust and to open the reverser cascades for flow redirection. Tailpipe blockage is accomplished by blocking doors hinged to the translating ring. Engine thrust is controlled from the engine throttle console. The reverse thrust lever is hinged to the forward thrust lever as shown in the schematic of Figure 10. On the 747 airplane, a lockout provision in the thrust lever assembly prevents simultaneous activation of the forward and reverse thrust levers. To obtain reverse thrust, the forward thrust lever must be in the idle position. The

reverse thrust lever is then moved upward to the reverse idle position. A linear time delay is required for the thrust to change from forward idle to reverse idle with no change taking place in the engine parameters (EPR, EGT, etc.).

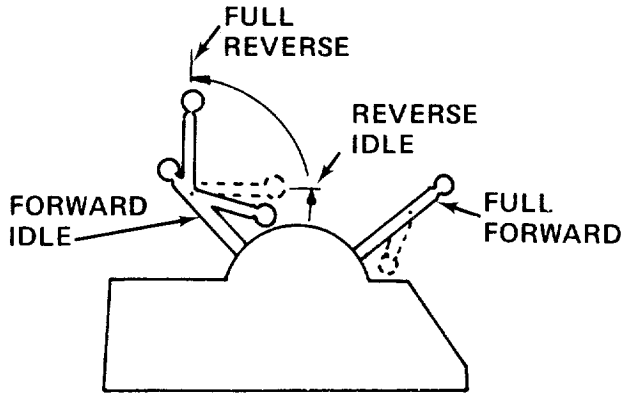

ENGINE THROTTLE CONSOLE

FIGURE 10

NASA Propulsion Model and Approximations

Engine pressure ratio was computed from the engine throttle angle as shown by the block diagram in Figure 11. The engine throttle angle was converted to engine power lever angle (fuel control angle at the engine). The hysteresis computation between the throttle angle and the power lever angle was neglected for the NASA simulation. The hysteresis in the physical mechanism of the NASA throttle mechanism was assumed to equal the hysteresis between the pilot's throttle and the fuel control on the actual airplane. The static EPR was computed as a function of ambient temperature (T_{AM}) for a known power lever angle. The static EPR was input to the NASA engine transient program. An incremental EPR (ΔEPR) was added to the output of the transient program to account for effects of altitude and Mach number. The 747 flight idle limiter was incorporated into the NASA simulation by increasing the actual EPR by a constant when the flaps were in the 25 or greater position and the landing gear was down but not on the ground.

JT9D-3 engine parameter time histories of fast and normal accelerations and decelerations for various airspeeds and altitudes were given to NASA. NASA's engine transient program was modified to approximate these characteristics. The time histories are included in Section 12, Volume II of this report.

The engine thrust simulation is shown in Figure 12. Forward net thrust was computed from EPR, Mach number and ambient pressure ratio. Reverse net thrust was assummed to be only a function of ambient pressure ratio and EPR since thrust reversers are only used from touchdown speed to 100 knots. The thrust mode (forward thrust or reverse thrust) depended upon the positioning of the throttle controls in the cab.

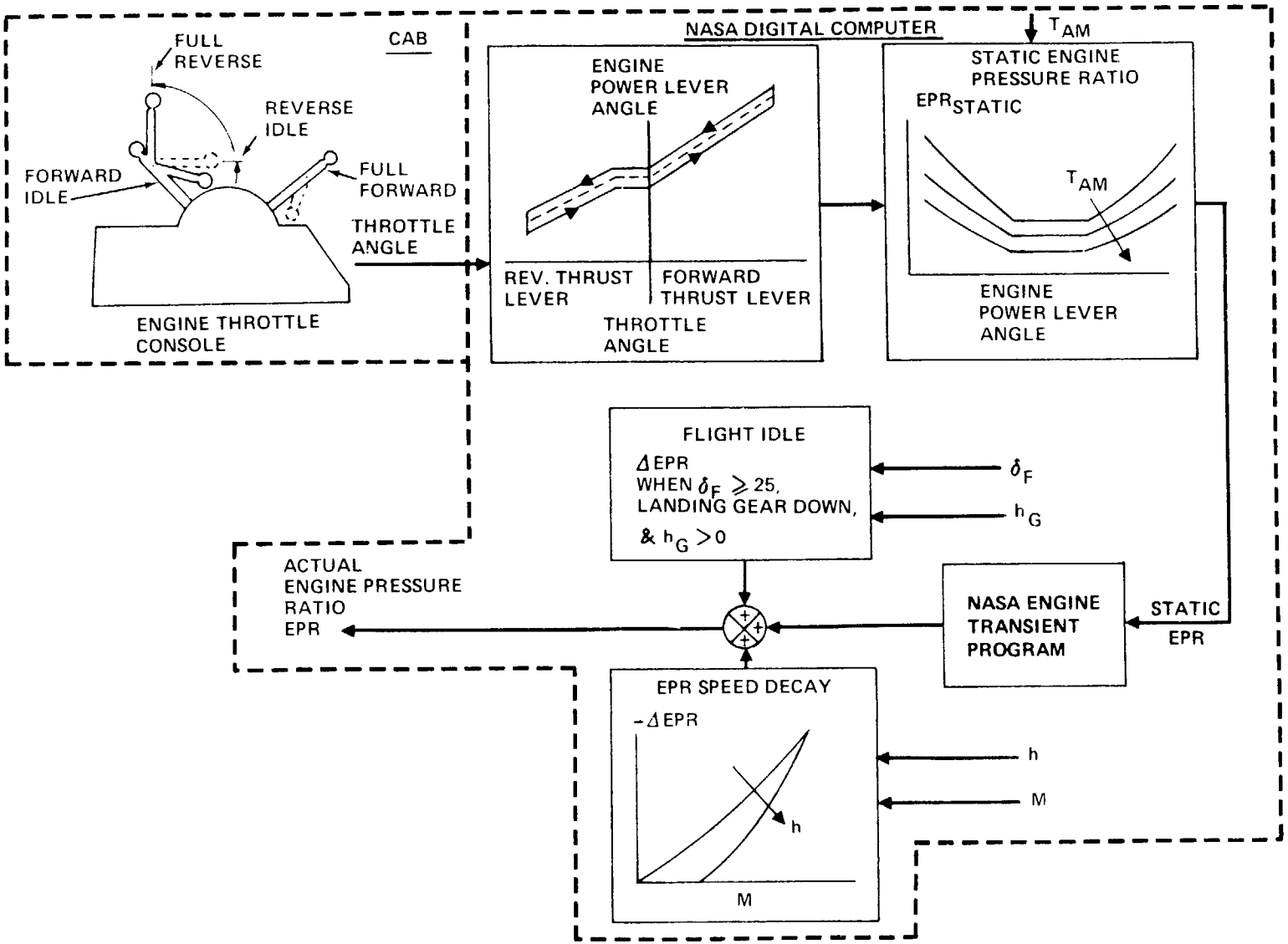

ENGINE PRESSURE RATIO SIMULATION

FIGURE 11

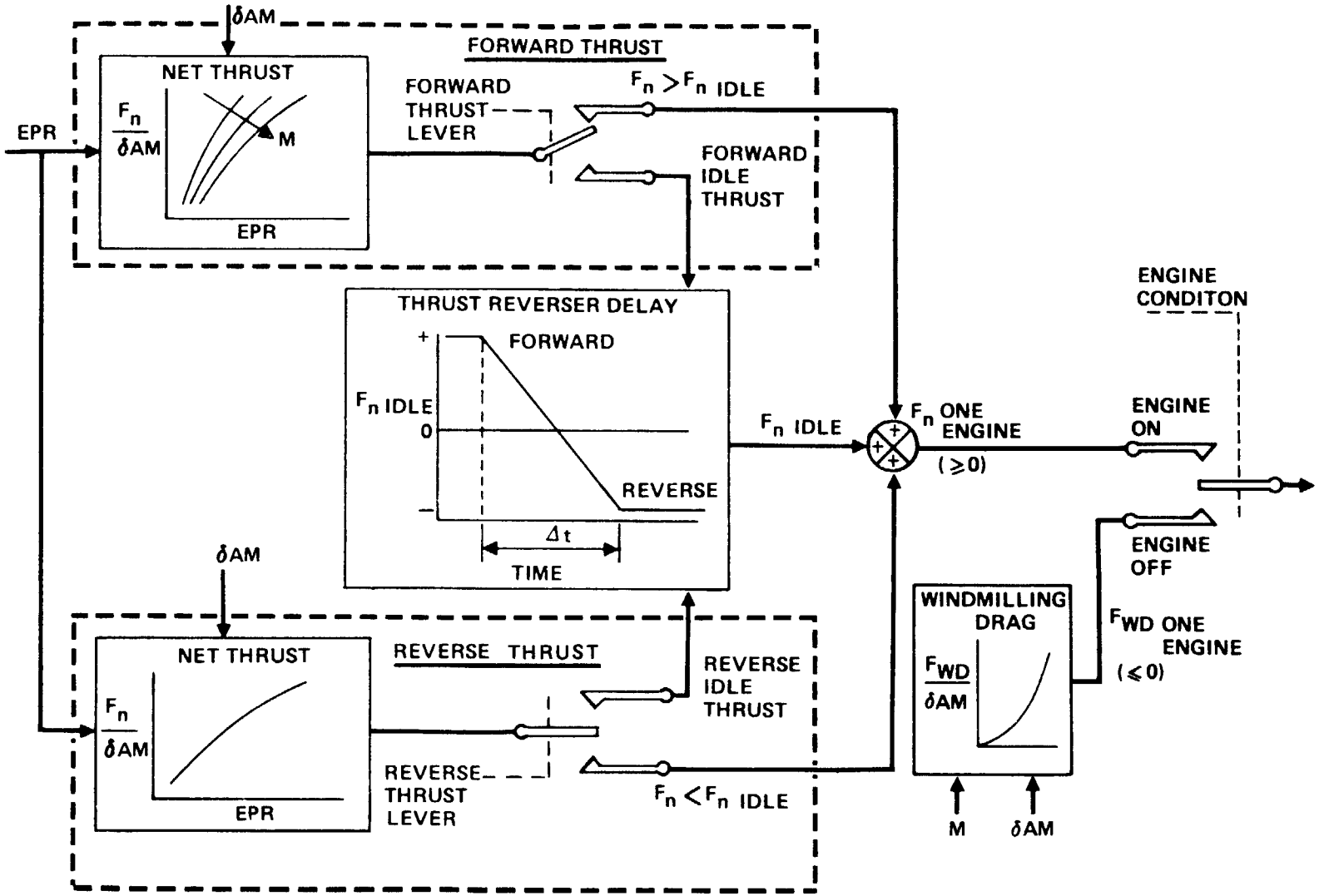

ENGINE THRUST SIMULATION

FIGURE 12

A linear transition with time was used to account for actuation of the thrust reverser mechanism when changing from forward idle thrust to reverse idle thrust.

The engine parameters displayed in the cab were EPR, exhaust gas temperature (EGT) and percent compressor RPM ($\%N_1$). A detailed method for generation of EGT and $\%N_1$ is shown in Figure 13. The temperature correction as a function of altitude was small and the compressor RPM was roughly proportional to the EGT data. Since the EGT and RPM gages were not essential to the simulation, approximations were made for the NASA simulation as shown in Figure 14.

The detailed 747 engine parameter data and the correlation of NASA thrust simulation data with actual engine data are included in Volume II of this report, Sections 12 and 14 respectively.

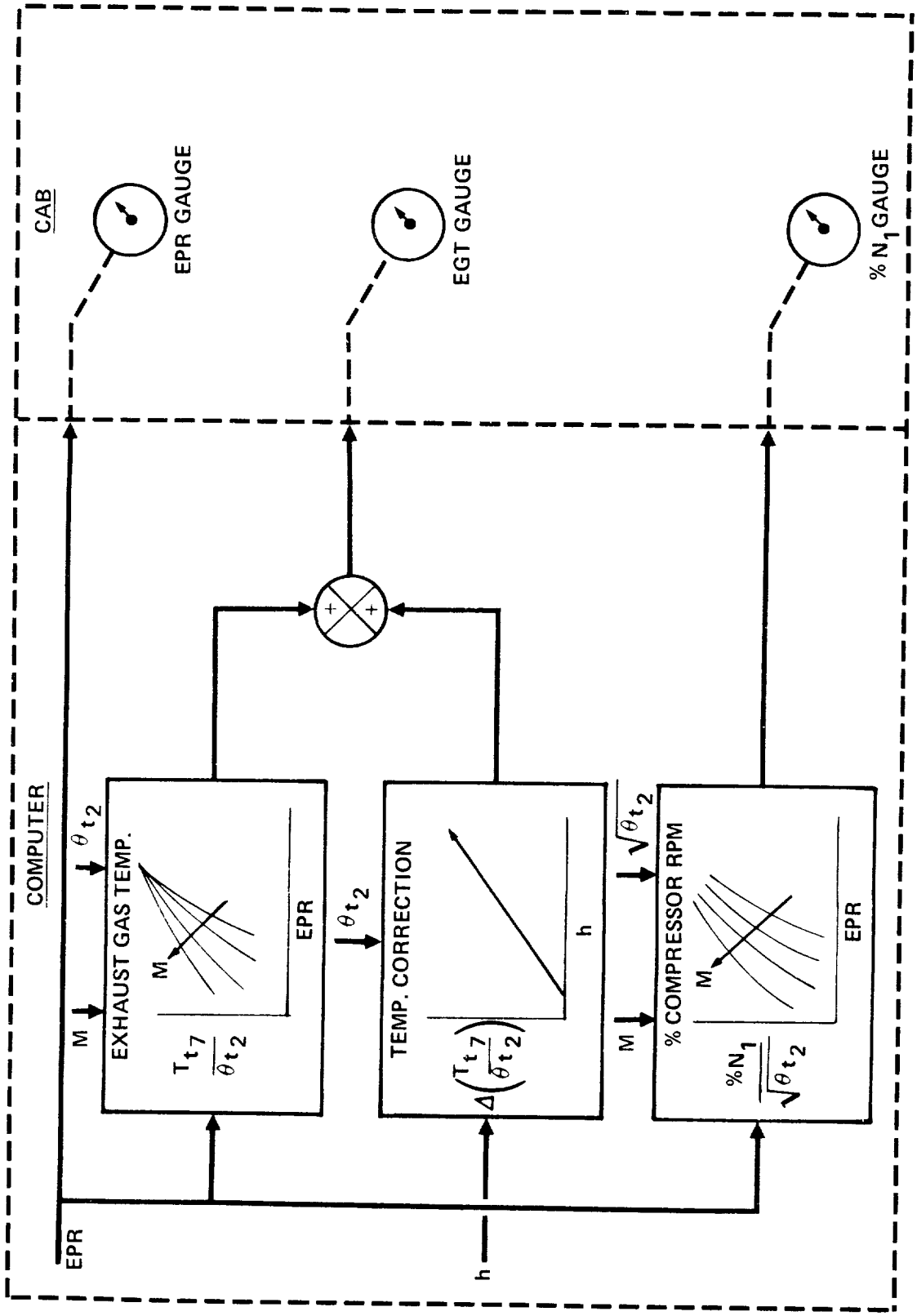

PARAMETERS FOR 747 ENGINE GAUGE DISPLAY
FIGURE 13

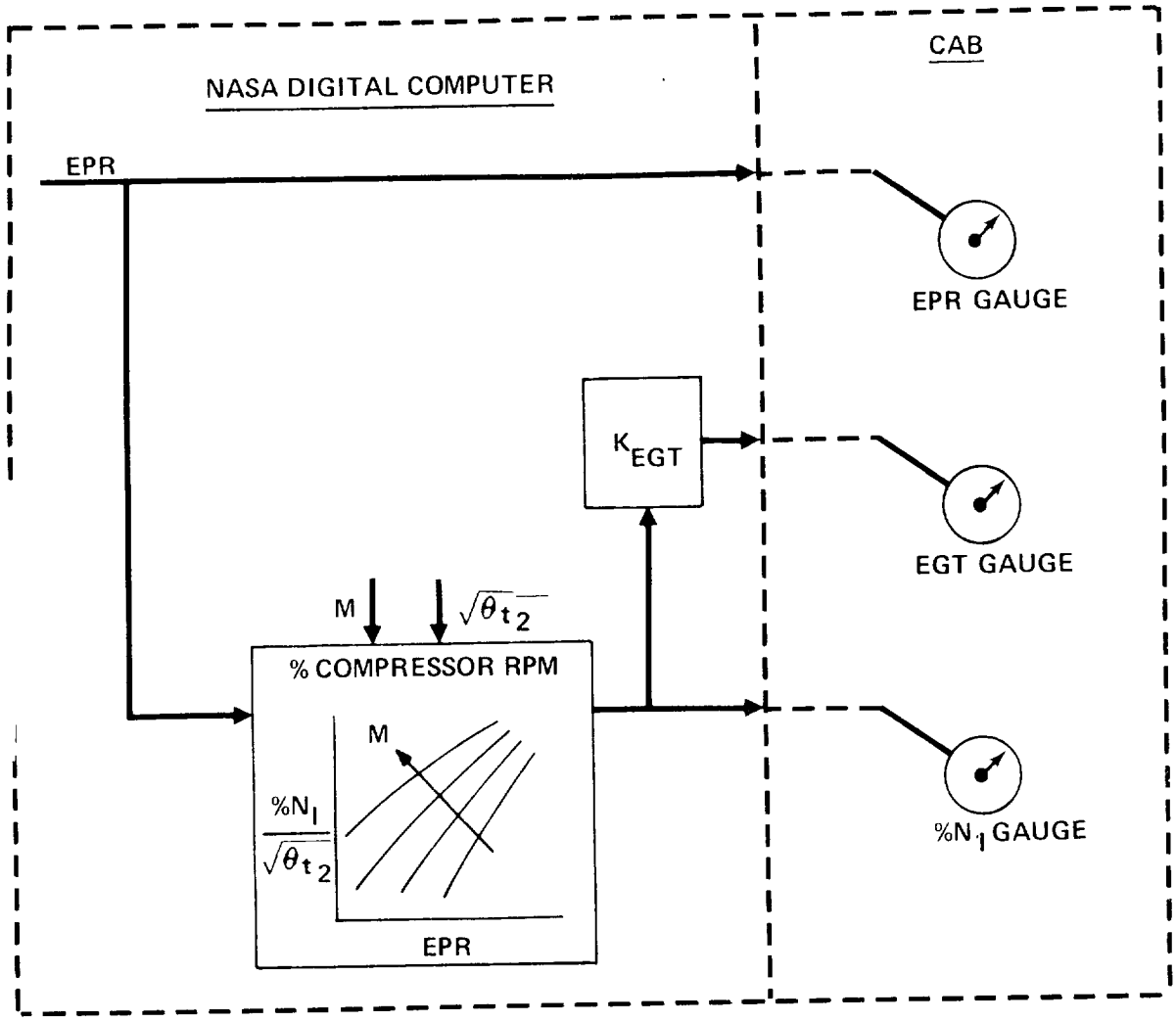

APPROXIMATIONS FOR NASA ENGINE GAUGE DISPLAY

FIGURE 14

LANDING GEAR SYSTEM

General Description

The 747 employs a four strut main landing gear system with a single strut nose gear, as illustrated in Figure 15.

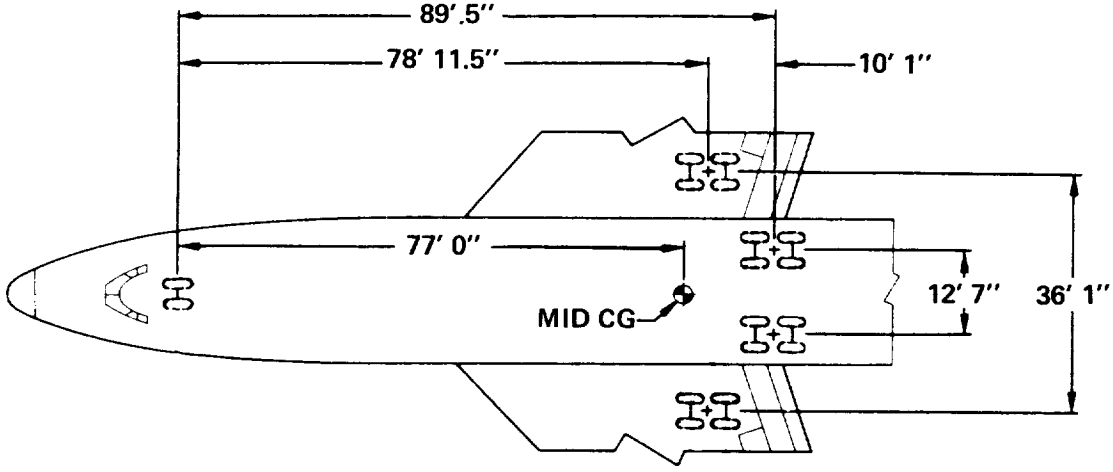

LANDING GEAR GEOMETRY

FIGURE 15

Two of the main gear struts are wing mounted and two are body mounted. Each main gear strut has a four-wheeled truck. The nose gear strut has two wheels. Because of the geometry of the wheel wells, the wing gear trucks are tilted upward 53 degrees after liftoff for retraction. The body gear trucks are tilted upward 7 degrees for retraction. Since the main landing gears are not aligned longitudinally, a load equalizer is employed to give an effective pitch rotation point midway between the wing and body gear struts.

Nose gear steering is controlled by a tiller and the rudder pedal controls. Full tiller deflection turns the nose gear 70 degrees. Full rudder-pedal travel turns the nose gear 10 degrees.

The rudder pedals command the braking system. A force of approximately 80 pounds is required to obtain maximum braking. Each wheel on the main gear struts is equipped with an anti-skid braking system.

NASA Landing Gear Model and Approximations

The following ground rules were used for the NASA simulation of the 747 landing gear system:

(1) The main body and wing gear struts were combined into an equivalent landing gear.

(2) Braking capability was provided on the equivalent main gear.

(3) Nose wheel steering as a function of rudder pedal travel was incorporated. Nose wheel

steering with a tiller was incorporated but not calibrated to the airplane.

(4) All forces generated by the landing gear contacting the runway were resolved into body axes forces and moments for computation of the airframe response.

(5) Small angle approximations were used for computing landing gear compression, compression rate, and body axes force and moment resolution.

(6) The NASA landing gear simulation was used wherever possible.

The equivalent landing gear model is shown in Figure 16.

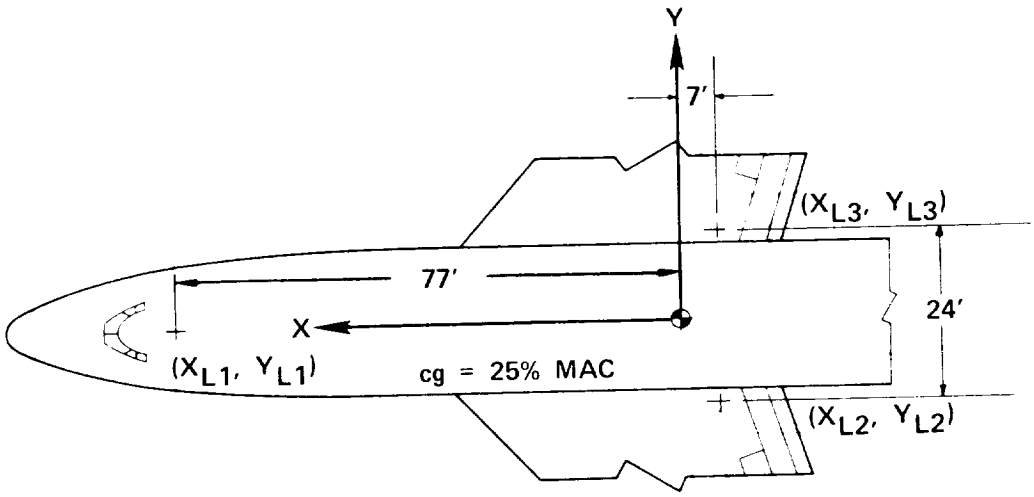

EQUIVALENT LANDING GEAR

FIGURE 16

The subscripts 1 through 3 denote the nose gear, main left gear, and main right gear respectively. The subscript "i" in the landing gear equations denotes application of the equation to simulate any one of the three landing gears.

Figures 17 through 20 show progressively in block diagram form the method used for computing landing gear forces and moments in the NASA simulation.

The distance from the c.g. to the landing gear struts was computed as a function of c.g. location as shown in Figure 17. Oleo strut compression (ΔS_{T_i}) was computed by knowing the height of the c.g. (h), the body pitch angle (θ_B), the body bank angle (ϕ_B), and the coordinates of the landing

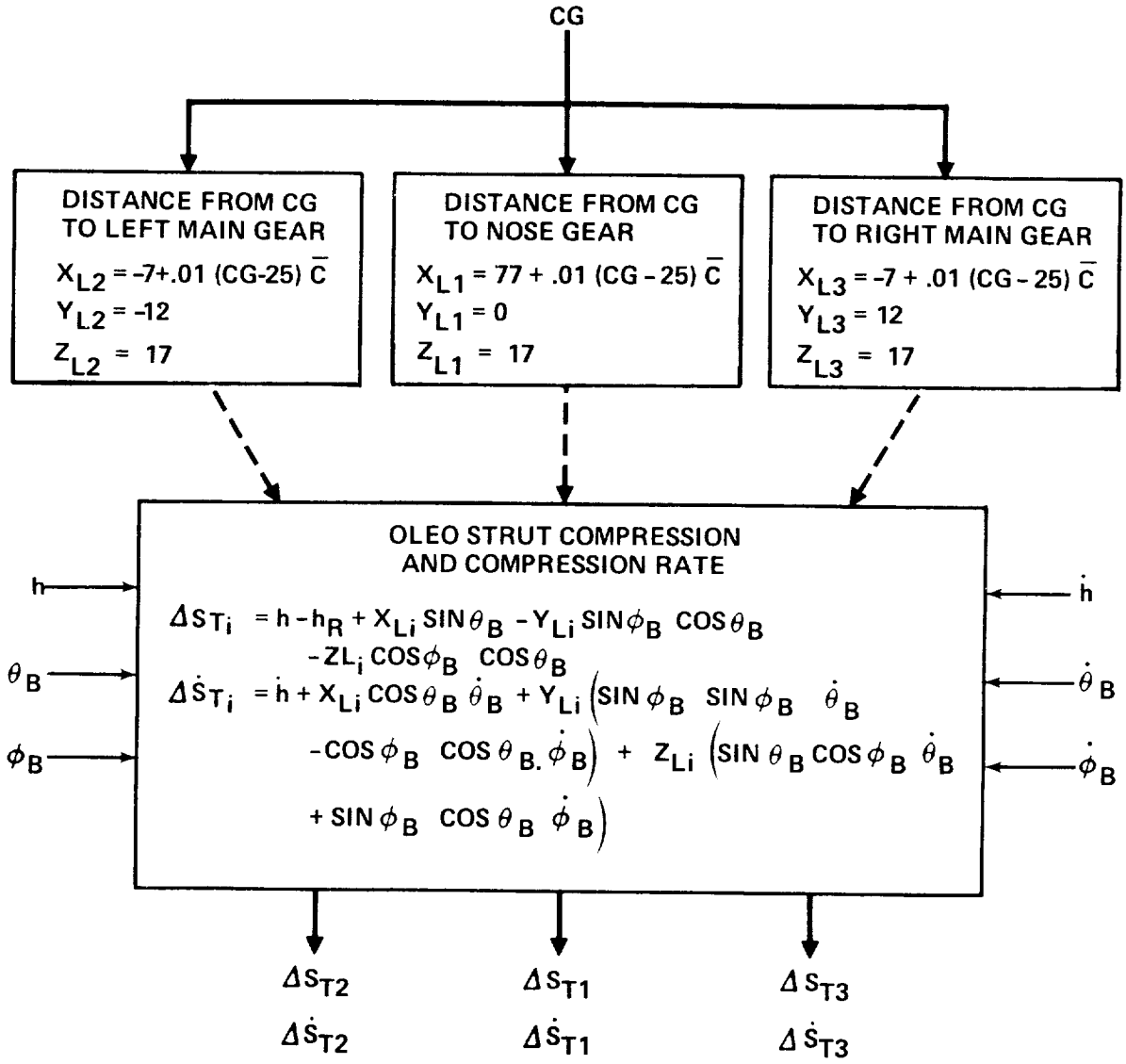

NOTE; LANDING GEAR DOES NOT CONTACT THE RUNWAY UNLESS $\Delta S_{Ti} < 0$

DETERMINATION OF OLEO STRUT COMPRESSION AND COMPRESSION RATE

FIGURE 17

gear struts. The oleo strut compression equation assumes small angle displacements. The equation for determining oleo strut compression (ΔS_{T_i}) is derived in its complete form in the Appendix. The rate of compression of the oleo strut ($\dot{\Delta S}_{T_i}$) was computed from the first derivative of the oleo strut compression equation.

The vertical oleo strut force (FG_Z) resulting from the oleo strut deflection and deflection rate were computed from the non-linear spring force and damping constant data as illustrated in the block diagram of Figure 18. Data for the spring force and damping constant parameter for the equivalent main landing gear and the nose gear are included in Section 13, Volume II, of this report.

The normal force of the tire on the runway generated by the oleo strut force F_{G_Z} is

$$F_{N_G} = \frac{F_{G_Z}}{\cos \theta_B \cos \phi_B} \quad .$$

With small angle approximations, runway normal force and oleo strut force were assumed equal. The axes system for the forces generated by the tires on the runway and the relation of these forces to aircraft body axes are shown and derived in the Appendix of this report.

Figure 19 is a block diagram illustrating the method of computing wheel side force. Tire deflection (δ_T) was computed from the runway normal force multiplied by the tire deflection constant (K_T). Wheel side force (F_s) was computed from:

$$F_{si} = \left| G_{T_i} \delta_{T_i} - H_{T_i} \delta_{T_i}^2 \right| (\delta s - \beta_G) \text{ Where}$$

β_G = airplane side slip angle relative to ground velocity vector

δ_S = nose wheel steering angle (i = 1 only).

The nose wheel steering angle was calculated from rudder pedal deflection (δ_p) when the aircraft was on the runway. The constants G_{T_i} and H_{T_i} and the nose wheel steering gearing constant $\frac{\partial \delta s}{\partial \delta p}$ are included in Section 13, Volume II of this report.

Limiting side force on the wheels was computed from the wheel normal force and a coefficient of sliding friction of 0.6.

Wheel drag force was determined from the rolling coefficient of friction and brake application as shown in the block diagram of Figure 20. Braking was available on the main gear only. The rolling coefficient of friction of 0.015 was assumed in addition to a breakout coefficient of friction varying from .014 at zero ground speed to 0 at 10 knots ground speed. The resultant coefficient of friction was combined with the wheel normal force F_N to obtain the gear drag with no braking. Braking was obtained by multiplying brake pedal deflection (δ_B) by a braking constant K_B and the aircraft mass (W/g). The braking force was limited to:

$$(F_{B_i})_{max} = \mu_B K_{BM} \frac{W}{g}$$

where the value of μ_B depended on the condition of the runway. Braking constants and gearing are included in Section 13, Volume II of this report. Brake and rolling friction are added to obtain the total retarding force on the tire.

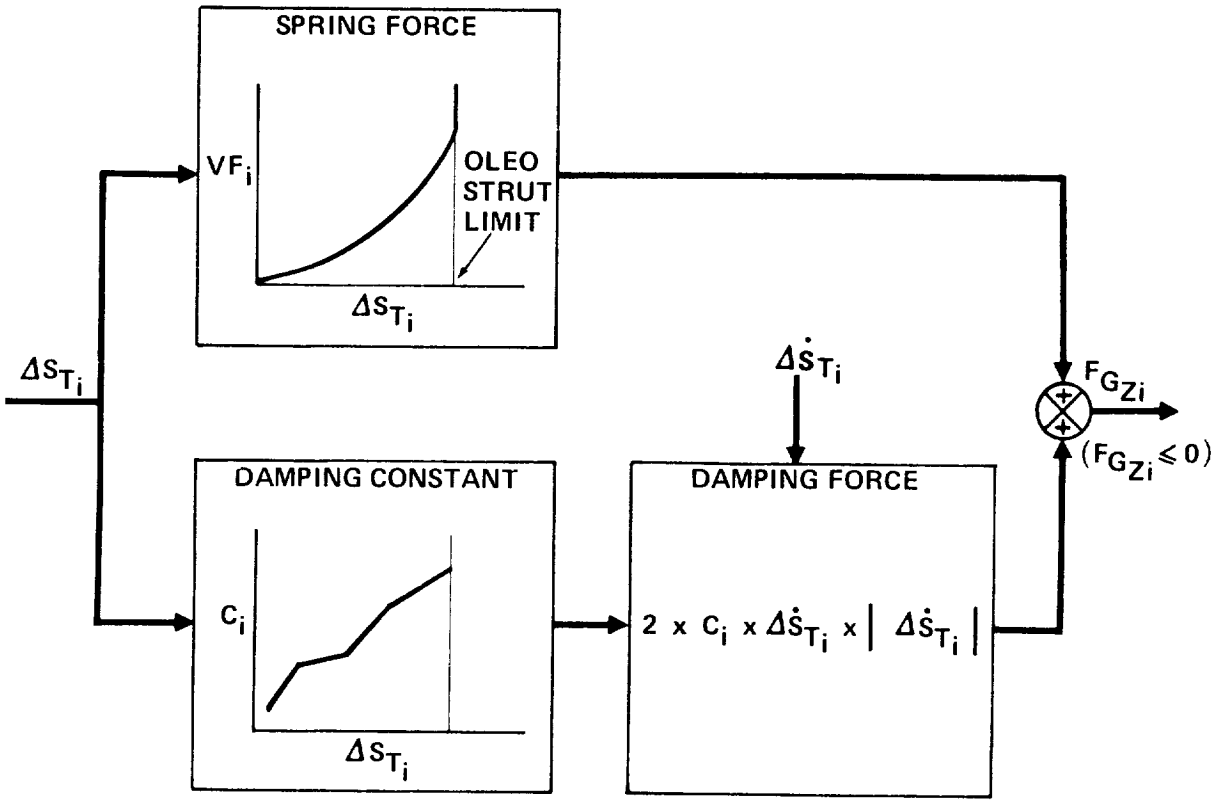

DETERMINATION OF OLEO STRUT FORCES

FIGURE 18

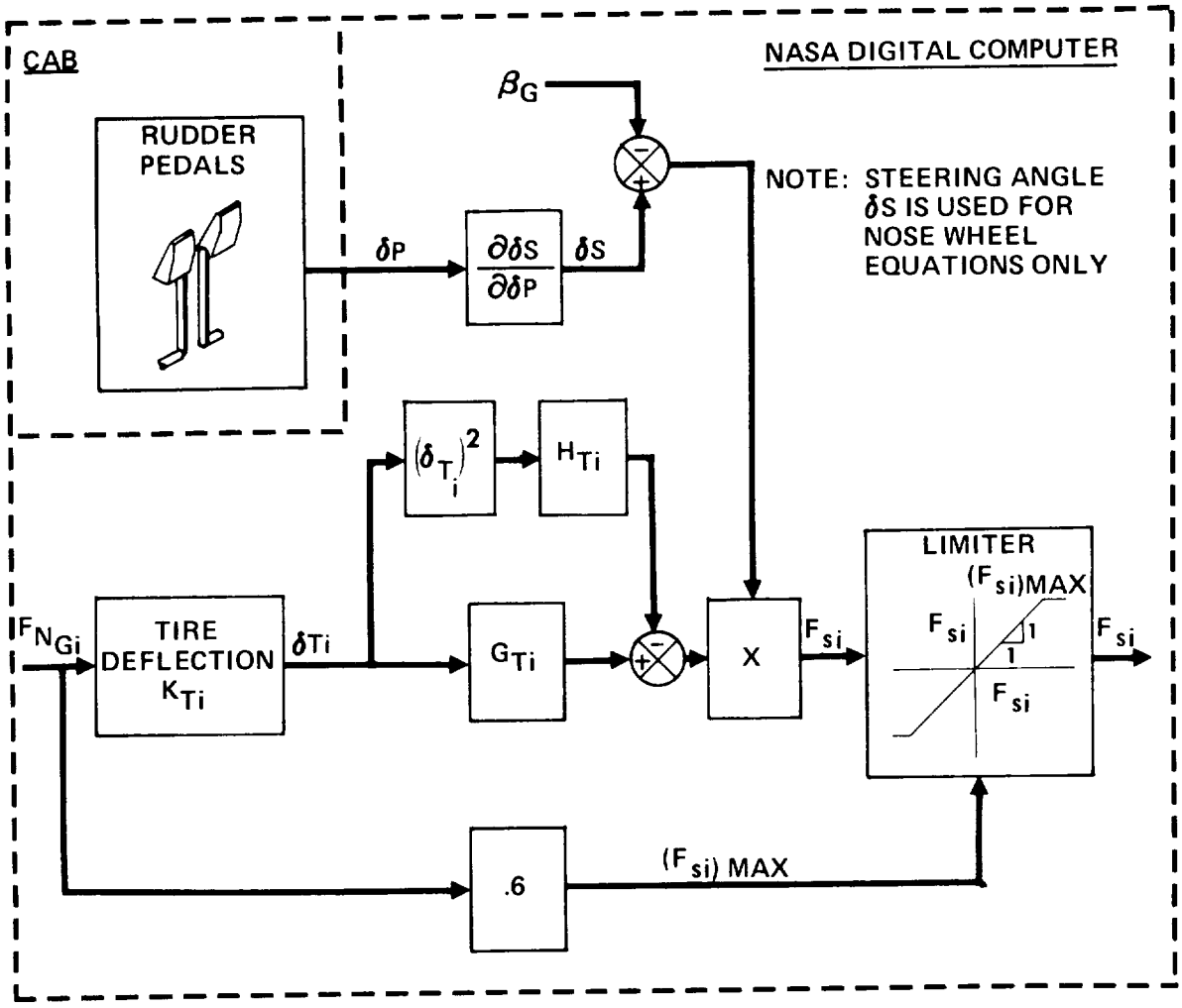

DETERMINATION OF WHEEL SIDE FORCE

FIGURE 19

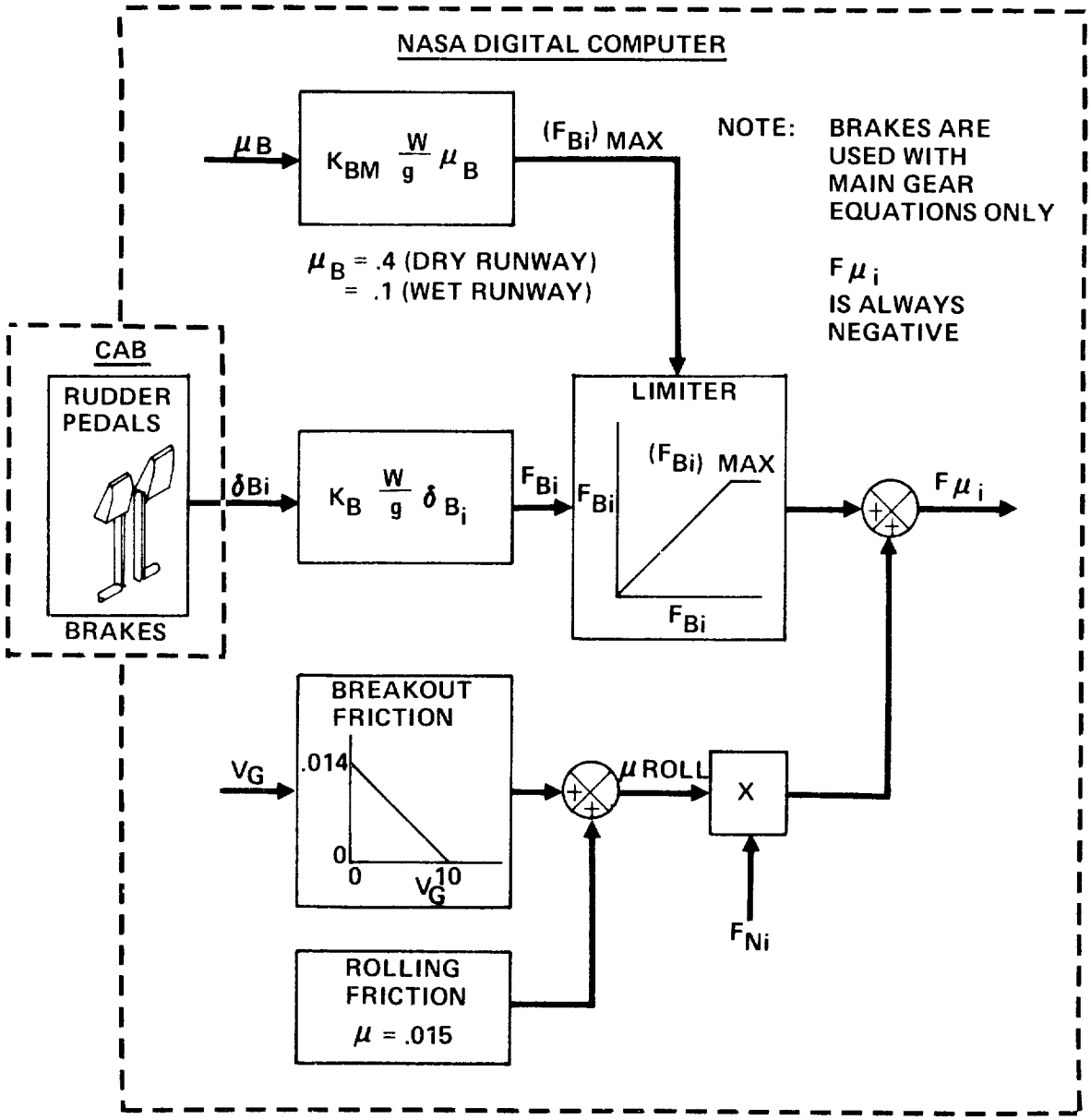

DETERMINATION OF WHEEL DRAG FORCE

FIGURE 20

Tire normal force, side force, and drag force were computed for each individual oleo strut and resolved into body axes by:

$$F_{RX_{Pi}} = F_{\mu i} - F_{G_{Zi}} \theta_B \quad \text{(FOR MAIN GEAR, i = 2,3)}$$

$$F_{RX_{Pi}} = F_{\mu i} - F_{G_{Zi}} \theta_B - F_{si} \delta_S \quad \text{(FOR NOSE GEAR, i = 1)}$$

$$F_{RY_{Pi}} = F_{si} + F_{G_{Zi}} \phi_B$$

$$F_{RZ_{Pi}} = F_{\mu i} \theta_B - F_{si} \phi_B + F_{G_{Zi}} .$$

The forces exerted on the aircraft through the oleo struts are obtained by summing the partial body axes forces.

$$F_{RX} = \sum_{i=1}^{3} F_{RX_{Pi}}$$

$$F_{RY} = \sum_{i=1}^{3} F_{RY_{Pi}}$$

$$F_{RZ} = \sum_{i=1}^{3} F_{RZ_{Pi}}$$

The vertical distance from the c.g. to the normal force, side force, and drag force vectors created by the tires in contact with the runway is

$$h_{Bc.g.i} = 17 + \Delta S_{T_i} .$$

Body axes moments were computed from the partial body axes forces and the distance from the c.g. to the runway.

$$M_{RX} = \sum_{i=1}^{3} (F_{RZ_{Pi}} Y_{Li} - F_{RY_{Pi}} h_{Bc.g.i})$$

$$M_{RY} = \sum_{i=1}^{3} (-F_{RZ_{Pi}} X_{Li} + F_{RX_{Pi}} h_{Bc.g.i})$$

$$M_{RZ} = \sum_{i=1}^{3} (F_{RY_{Pi}} X_{Li} - F_{RX_{Pi}} Y_{Li})$$

ATMOSPHERE MODEL

The ICAO standard atmosphere model was used to simulate the atmosphere's physical properties throughout the flight envelope of the 747. Table 2 shows the equation used to compute atmospheric temperature ratio (θ) and pressure ratio (δAM).

ICAO Standard Atmosphere

ALTITUDE <36,089 FT	ALTITUDE >36,089 FT
$\theta = \frac{T}{T_o} = 1\text{-}6.875 \times 10^{-6} h$	$\theta = \frac{T}{T_o} = .7518$
$\delta AM = \frac{P}{P_o} = \theta^{5.256}$	$\delta AM = \frac{P}{P_o} = .2234e^{-4.806 \times 10^{-5}(h - 36{,}089)}$

TABLE 2

The sea level standard pressure, temperature, and speed of sound are

$$P_o = 2116.2 \text{ LB/FT}^2$$

$$T_o = 518.7^o \text{ R}$$

$$a_o = 1116.4 \text{ FT/SEC}.$$

AIRSPEED EQUATIONS

The speed of sound (ft/sec) was determined from $a = 1116.4\sqrt{\theta}$. Mach number was computed from the true airspeed obtained from the airframe equations of motion,

$$M = \frac{V}{a}.$$

The compressible dynamic pressure was computed by

$$q_c = 2116.2 \quad \delta AM \left[(1 + .2M^2)^{3.5} - 1\right] \quad \text{LB/FT}^2$$

from which calibrated airspeed was computed,

$$V_c = \left\{2{,}187{,}745\left[\left(\frac{q_c}{2116.2} + 1\right)^{2/7} - 1\right]\right\}^{1/2} \quad \text{KNOTS}.$$

SIMULATION CHECKOUT

The mathematical models and data of the 747 aircraft were qualitatively and quantitatively checked to substantiate the accuracy and validity of the NASA FSAA simulation. The checkout included verification of the aerodynamic forces and moments, the solution of the equations of motion, and the simulation of flight control system characteristics. Checkout consisted of non-pilot and piloted static and dynamic flight conditions as well as an overall piloted assessment of the simulation. The quantitative results were compared to Boeing simulator and flight test data.

Quantitative non-piloted simulation checkout included the following:

1. Cockpit instruments
2. Atmosphere model
3. Engine characteristics
    a. Forward thrust
    b. Reverse thrust
    c. Transient response
4. Longitudinal trim
5. Configuration changes (trim)
    a. Flaps
    b. Landing gear
    c. Speed brakes
    d. Ground effect
6. Elevator stabilizer trades
7. Dynamics
    a. Short period
    b. Phugoid
    c. Dutch roll
8. Flight controls
    a. Force and displacement

b. Rigging

c. Blowdown

The piloted evaluation of the simulation was conducted by a Boeing and a NASA pilot. The Boeing pilot flew the motion simulator for a total of 5 hours in 3 sessions. The NASA pilot assisted in obtaining the quantitative data as well as becoming familiar with the 747 characteristics.

Piloted simulation checkout included:

A. General qualitative assessment of the following:

1. Airplane handling characteristics

a. Dutch roll mode

b. Spiral mode

c. Short period mode

d. Phugoid mode

e. Roll rate

f. Climb performance

g. Flap extension and retraction

h. Speed brakes

2. Engine response

3. Ground effect

4. Control forces

5. Takeoff (3 and 4 engine)

6. Landing

7. Stall

8. Air minimum control speed

9. Buffet

10. Stick shaker

B. Quantitative evaluation of the following:

1. Takeoff time
2. Climb performance
3. Acceleration and deceleration times in the air
4. Steady turns (elevator and stick force per g)
5. Longitudinal static stability
6. Steady sideslips
7. Roll rates
8. Air minimum control speed

The quantitative results are documented in Section 14, Volume II of this report. In addition to the test data, the pilot comments substantiated the accuracy of the simulation.

APPENDIX - DERIVATION OF LANDING GEAR EQUATIONS

Gear Height

The complete equations for determining landing gear height are derived by methods of descriptive geometry as illustrated in Figure 21.

Let the coordinates of the axle of the strut be X_L, Y_L and Z_L and r be the tire radius. With zero bank angle, pitch the aircraft about the c.g. to an angle θ_B as shown in the side view of Figure 21. The height of the tire relative to the c.g. due to the pitch angle θ_B is

$$h_\theta = X_L \text{ SIN } \theta_B - Z_L \text{ COS } \theta_B - r.$$

After the pitch rotation θ_B, view the aircraft as shown in the rear view of Figure 21 and bank the aircraft to ϕ_B. In the rear view the change in vertical distance from the c.g. to tire is

$$Y_L \text{ SIN } \phi_B + (Z_L + r) \text{ COS } \phi_B - (Z_L + r).$$

Resolving this displacement of the tire relative to the c.g. from the rear view to the side view and into a change in height gives

$$h_\phi = \left[Y_L \text{ SIN } \phi_B + (Z_L + r) \text{ COS } \phi_B - (Z_L + r)\right] \text{ COS } \theta_B$$

or

$$h_\phi = \left[Y_L \text{SIN } \phi_B + (Z_L + r) \text{ (COS } \phi_B - 1)\right] \text{ COS } \theta_B.$$

In the NASA simulation $(Z_L + r)$ is replaced by an equivalent distance S_z. This simplification assumes the tire will contact the runway at a point aligned with the oleo strut as illustrated in Figure 22.

The total height of the tire above the runway is then given by

$$h_G = h + h_\theta - h_\phi.$$

If h_G is negative, the gear will be in contact with the runway and the oleo strut compression ΔS_T is obtained from

$$\Delta S_T = h_G \Big/ \text{COS } \theta_B \text{ COS } \phi_B.$$

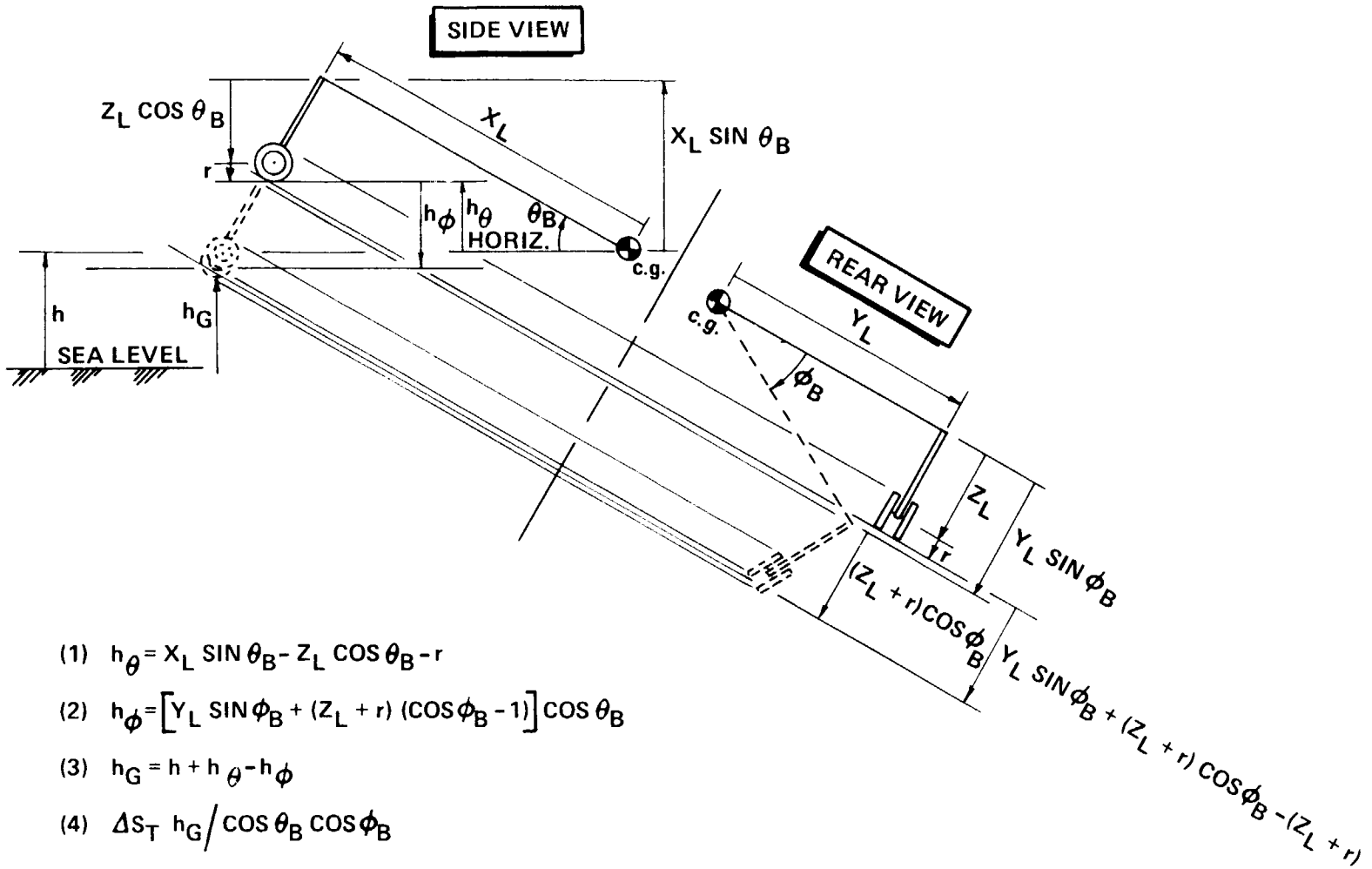

(1) $h_\theta = X_L \sin \theta_B - Z_L \cos \theta_B - r$

(2) $h_\phi = \left[Y_L \sin \phi_B + (Z_L + r)(\cos \phi_B - 1)\right] \cos \theta_B$

(3) $h_G = h + h_\theta - h_\phi$

(4) $\Delta S_T \; h_G \Big/ \cos \theta_B \cos \phi_B$

DERIVATION OF EQUATIONS FOR DETERMINING GEAR HEIGHT

FIGURE 21

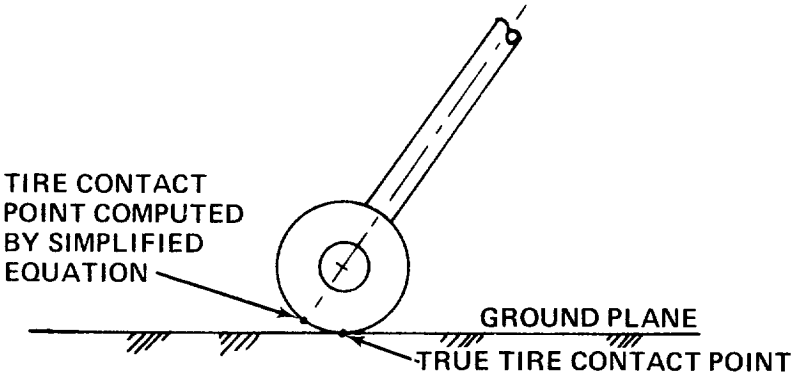

WHEEL RUNWAY CONTACT
FIGURE 22

Tire Forces

The orthogonal forces generated by a tire in contact with the runway are shown in Figure 23.

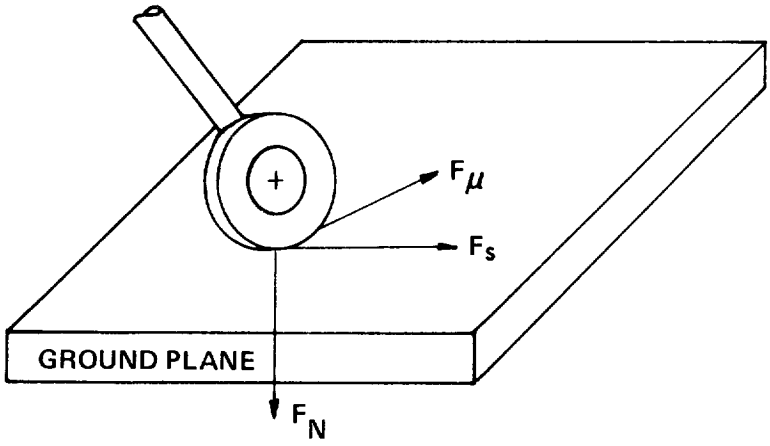

FIGURE 23

The tire drag force vector F_μ is aligned by the intersection of a plane through the tire tread and the ground plane. The normal force vector, F_N, is perpendicular to the ground plane. The side force, F_S, generated by the tire is perpendicular to the plane containing F_μ and F_N. The tire forces are resolved through the aircraft pitch attitude θ_B and bank angle ϕ_B to obtain the body axes forces exerted on the aircraft. The resultant forces in body axes are derived by descriptive geometry methods as illustrated in Figure 24 for normal force, F_N, and in Figure 25 for drag force, F_μ, and side force, F_S .

In the side view of Figure 24, prior to any axes rotation, the normal force vector F_N acts downward, perpendicular to the ground plane. If the aircraft is pitched through an angle θ_B , the normal force in body axes due to the pitch rotation is

$$F_{X_{B_\theta}} = -F_N \sin \theta_B$$

$$F_{Y_{B_\theta}} = 0$$

$$F_{Z_{B_\theta}} = F_N \cos \theta_B$$

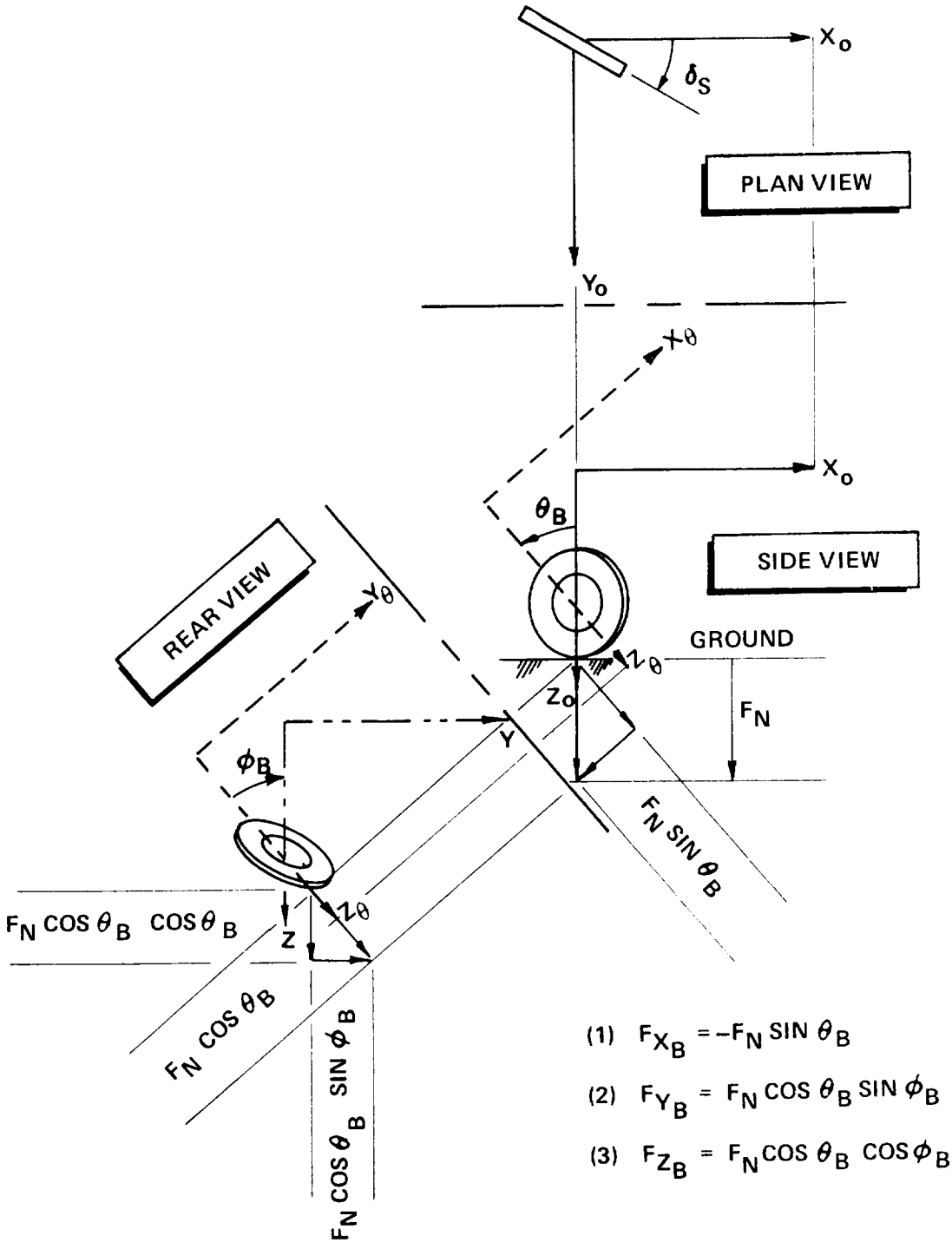

RESOLUTION OF WHEEL NORMAL FORCE INTO AIRPLANE BODY AXES

FIGURE 24

If the aircraft is viewed from the rear, as shown by the rear view of Figure 24, and is rotated through a bank angle ϕ_B, the normal force in body axes is

$$(1)\quad F_{X_B} = -F_N \sin \theta_B$$

$$(2)\quad F_{Y_B} = F_N \cos\theta_B \sin\phi_B$$

$$(3)\quad F_{Z_B} = F_N \cos\theta_B \cos\phi_B$$

Equations (1) through (3) represent the resolution of the normal force into body axes.

In the plan view of Figure 25, prior to any axes rotation, the gear drag force acts in the direction of tire rotation and the side force acts perpendicular to the side of the tire. The wheel steering angle is δ_S. The forces resolved into body axes are

$$F_{X_{B_o}} = F\mu \cos \delta_s - F_s \sin \delta_s$$

$$F_{Y_{B_o}} = F\mu \sin \delta_s + F_s \cos \delta_s$$

$$F_{Z_{B_o}} = 0$$

If the aircraft is pitched through an angle θ_B, as shown in the side view of Figure 25, the forces resolved in body axes are

$$F_{X_{B_\theta}} = (F\mu \cos \delta_s - F_s \sin \delta_s) \cos \theta_B$$

$$F_{Y_{B_\theta}} = F\mu \sin \delta_s + F_s \cos \delta_s$$

$$F_{Z_{B_\theta}} = (F\mu \cos \delta_s - F_s \sin \delta_s) \sin \theta_B$$

The bank angle axes rotation as shown in the rear view of Figure 25 gives the final value of wheel drag and side force in body axes as

$$(4)\quad F_{X_B} = (F\mu \cos \delta_s - F_s \sin \delta_s) \cos \theta_B$$

$$(5)\quad F_{Y_B} = (F\mu \sin \delta_s + F_s \cos \delta_s) \cos \phi_B + (F\mu \cos \delta_s - F_s \sin \delta_s) \sin \theta_B \sin \phi_B$$

$$(6)\quad F_{Z_B} = -(F\mu \sin \delta_s + F_s \cos \delta_s) \sin \phi_B + (F\mu \cos \delta_s - F_s \sin \delta_s) \sin \theta_B \cos \phi_B$$

Equations (4) through (6) when combined with Equations (1) through (3) represent the forces in aircraft body axes generated by a tire contacting the runway.

For the NASA simulation, small angle approximations were used to resolve the forces into body

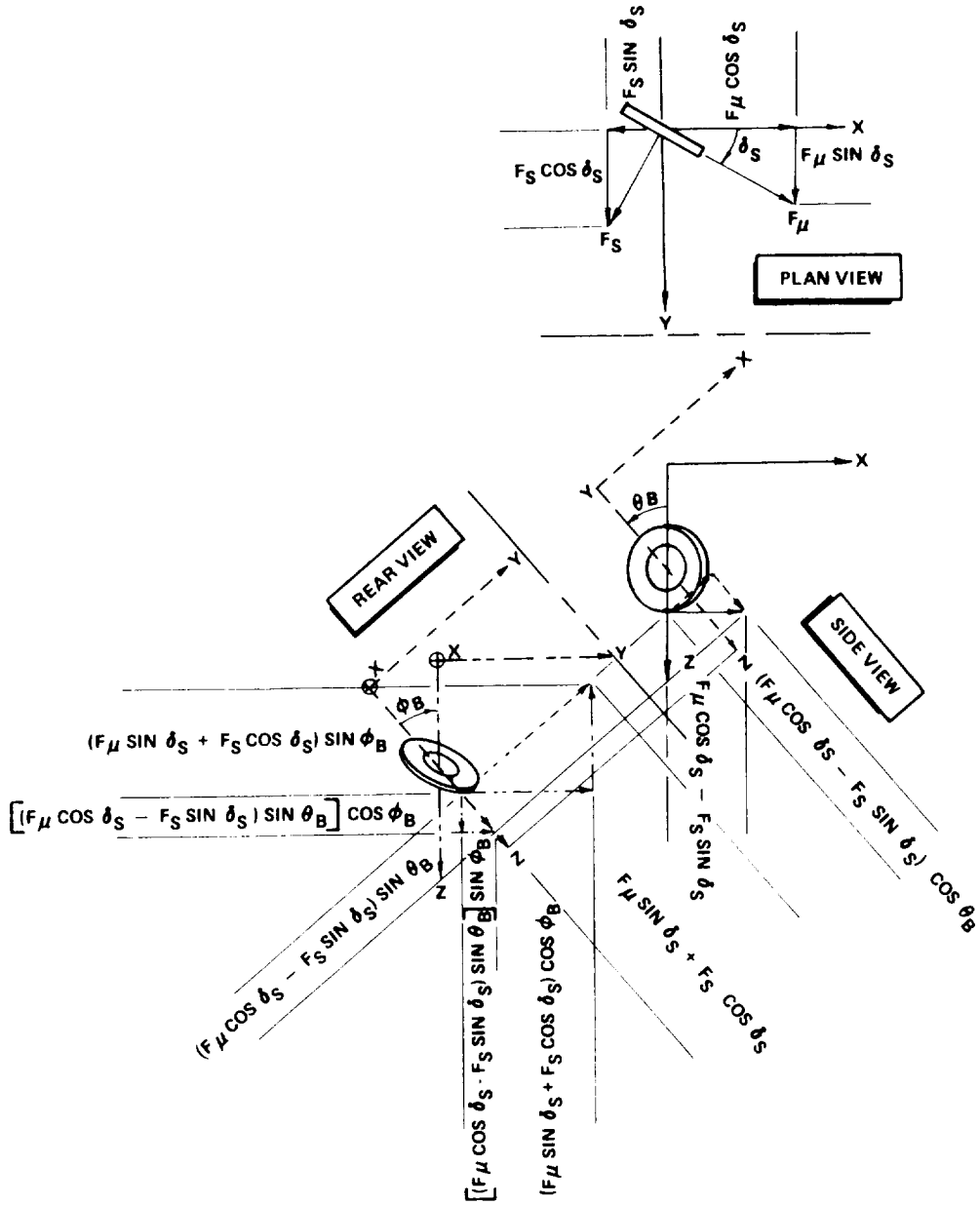

(1) $F_x = (F_\mu \cos \delta_S - F_S \sin \delta_S) \cos \theta_B$

(2) $F_y = (F_\mu \sin \delta_S + F_S \cos \delta_S) \cos \phi_B + (F_\mu \cos \delta_S - F_S \sin \delta_S) \sin \theta_B \sin \phi_B$

(3) $F_z = -(F_\mu \sin \delta_S + F_S \cos \delta_S) \sin \phi_B + (F_\mu \cos \delta_S - F_S \sin \delta_S) \sin \theta_B \cos \phi_B$

RESOLUTION OF WHEEL DRAG AND SIDE FORCE INTO AIRPLANE BODY AXES

FIGURE 25

axes. The normal force Equations (1) through (3) were simplified to

$$(7)\quad F_{X_B} = -F_N \theta_B$$

$$(8)\quad F_{Y_B} = F_N \phi_B$$

$$(9)\quad F_{Z_B} = F_N = F_{G_Z}$$

where F_{G_Z} = forces generated by compression of the oleo strut.

The drag force equations (4) through (6) were simplified to

$$(10)\quad F_{X_B} = F\mu - F_s \delta_s$$

$$(11)\quad F_{Y_B} = F\mu\ \delta_s + F_s$$

$$(12)\quad F_{Z_B} = -F_s \phi_B + F\mu \theta_B$$

Combining Equations (7) through (12) gives the final equations used for the NASA simulation

$$F_{X_B} = F\mu - F_s \delta_s - F_{G_Z} \theta_B$$

$$F_{Y_B} = F\mu\ \delta_s + F_s + F_{G_Z} \phi_B$$

$$F_{Z_B} = F\mu\ \theta_B - F_s \phi_B + F_{G_Z}$$

NASA-Langley, 1971 —— 2